



# Optimization of NbTiN thin film sputtering and optical lithography for large area superconducting nanowire single photon detectors


## CANDIDATE

Marco Zagarella

## SUPERVISORS

Prof. Karl Berggren
Prof. Renato Gonnelli


**Master's Degree Thesis**

Master's Degree in Nanotechnologies for ICTs
Micro and Nanotechnologies for Integrated Systems


Politecnico di Torino - Grenoble INP Phelma - École polytechnique fédérale de Lausanne

# Abstract

Superconducting nanowire single photon detectors (SNSPDs) are the state-of-the-art technology for time-resolved single-photon counting from the ultraviolet (UV) to the near-infrared. The recent discovery of single-photon sensitivity in micrometer-scale superconducting wires is a promising pathway to explore for large active area devices with application to dark matter searches and fundamental high-energy physics. On the other hand, incorporating a micron-scale wires as photo-sensitive element in SNSPDs can lead to significant improvements in their speed, footprint, and fabrication yield. However, the current application of Superconducting Microwire Single Photon Detectors (SMSPDs) has resulted in a decline in the detectors' intrinsic detection efficiency. The issue of low detection efficiency can be addressed through utilization of high-resistivity films. In this work the optimization of sputtering and fabrication process, based on optical lithography, for highly-resistive NbTiN are proposed. In this work, a single pixel detector, $300 \times 300$ µm$^2$ SMSPD with 1 µm-wide wires fabricated from high-resistivity NbTiN film (409 µΩ cm, with critical temperature comparable to bias-sputtered NbN) using maskless optical lithography. The device made from different thicknesses and critical temperatures of NbTiN did not show saturated internal detection efficiency at 3 K. By further optimizing the process techniques presented in this work, a viable pathway exists to realize large-areas devices with saturated internal detection efficiency.

*To my parents*

# Acknowledgements

This endeavor could not have reached fruition without the enduring support of my family, friends, and colleagues. I seize this moment to express my heartfelt gratitude to some of them.

First and foremost, I would like to express my deepest gratitude to my supervisor, Prof. Karl K. Berggren, whose expertise, understanding, and patience, added considerably to my graduate experience. I appreciate your mentorship and the time you invested in my research. Thanks for creating an environment which promotes scientific growth.

To my mentor Owen Medeiros, who has taught me all the experimental and theoretical know-how, thanks for pushing me to be a better scientist and for being a good friend. I will never forget all the help, ideas and suggestions you have given me throughout my visiting time. Your work ethic and mindset will take you very far.

To the Italian core of the QNN group, Marco Colangelo and Matteo Castellani, for introducing me to the QNN group and to Boston, my experience at MIT would have not been the same without you. I wish Marco Colangelo all the best for his future career as a professor (but I am sure he will do great things) and as a husband. I wish Matteo Castellani the best for his future and I thank him for organizing all the trips and for all the beers at Muddy.

To Francesca Incalza and Marco Raffa, thanks for being real friends and incredible roommates, who had the unlucky experience of spending every day of their stay with me.

My journey would not have been possible without the companionship and camaraderie of my friends who have stood by me through thick and thin. A special

thanks to Alessandro Buzzi, Davide Cassara' and Sofia Cerasi for the great moments, the laughter and the deep discussions.

I would also like to acknowledge the support from my peers in the QNN group: Emma Batson, Adina Bechhofer, Camron Blackburn, Reed Foster, Stewart A. Koppell, Dip Joti Paul, John Simonaitis and Matthew Yeung. Your collaborative spirit and camaraderie have made my time at QNN a rewarding experience.

Most of all to my family. I am deeply grateful to them, who have given me unwavering support throughout my academic journey. To my father and my mother, thank you for instilling in me the value of hard work and perseverance. Your love and sacrifices have been my pillar of strength. Without them I would not be the person I am today. To my brother, thank you for being my confidant and a source of inspiration. Your belief in my abilities means more than words can express.
To my grandparents, for keeping me well fed when coming back home and for the endless love they showed me.

Lastly, I extend my gratitude to all the authors and researchers whose works have informed and inspired this research. Your contributions to the field have been a guiding light in my scholarly journey.

In conclusion, I am thankful for this learning journey and the people who have been a part of it. This thesis not only stands as a testament to my hard work but also as a tribute to all who have supported me, believed in me, and invested in my potential.

*Thank you.*

# Contents

# Chapter 1

# Introduction

In the field of photonics, single photon detectors (SPDs) have emerged as indispensable tools, revolutionizing a wide range of applications by enabling the detection of individual photons. In the last decades, such level of resolution has opened up new frontiers in areas such as quantum communication [1], deep space communication [2], and sensing [3]. Among the various types of single photon detectors, the Superconducting Nanowire Single Photon Detectors (SNSPDs) have gained significant attention due their exceptional performance and today they represent the state-of-the-art for single photon detection in cryogenic setups.

The ability to detect and manipulate individual photons is of paramount importance in several cutting-edge technologies, such as quantum communication technologies, [4] and quantum computing. In quantum communication, SNSPDs allowed for several long-distance records for quantum key distribution [5, 6, 7]. In addition to quantum communication, single photon detectors find widespread use in optical imaging and biomedical imaging [8, 9].

## 1.1 Necessary theoretical background on superconductivity in nanowires and SNSPD

Before continuing with the main content of this work, a theoretical knowledge on superconducting nanowires (SNs) is provided for non-expertises, to allow best comprehension of this work and explain why SNSPDs play a fundamental role in single photon detection and why today they represent one of the most appealing technology in this field.

### 1.1.1 Superconductivity in nanowires

Superconducting nanowires (SNs) behave as a common metallic wires, when they are in their normal-state, i.e. above critical temperature, $T_c$. When they are cooled below their $T_c$ the resistance drops to zero, for low bias currents. An example of I-V curve is shown in Figure 1.1. This typical curve exhibits a pronounced hysteresis and the SN can be found in two distinct states: a superconducting state (SS) when the bias current is sufficiently low and the Joule-heated normal state (JNS). The SS is characterized by zero voltage drop across the ends of the SN, for working temperature lower than $T_c$. As the current is increased above a threshold value, which is commonly referred as critical (or switching) current, $I_c$ or $I_{sw}$ the voltage experiences a jump-wise transition to its normal state due to Joule heating effect. The resistance in its normal state is given by the Ohm law, $R_{ns} = R_s l/w$. Where $l$ and $w$ are the length and the width of the wire, while $R_s$ is known as sheet resistance and it is equal to $R_s = \rho/d$, where $\rho$ is the resistivity of the film and $d$ is the thickness. The value of $I_c$ depends on different parameters, such as working temperature, material and geometry of the SN, generally the critical varies from 10 µA up to few mA. The transition from JNS to SS occurs at a lower current, which is referred to retrapping current, $I_r$. $I_r$ is always lower than $I_c$ because, as the switching to JNS happens, the Joule heating increases from zero to a value of $R_{ns}\ I_c^2$, thus increasing the temperature of the wire much above $T_c$. Then, to bring the wire back to its SS the bias current needs to reach lower values than $I_c$.

### 1.1.2 Single photon detection in micrometer-wide wire

Since the discovery of superconducting nanowires single photon detectors in 2001, [10, 11], a complete theory of detection has not been presented yet. In Semenov et al. work a model for photon detection was published and generally referred as hotspot model. In this model, a single incident photon, with energy $E_{ph} = \hbar\omega \approx 1$ eV is able to break a Cooper pair if $E_{ph} > \Delta$, with $\Delta$ the superconducting gap, leading to the formation of an excited electron or quasiparticle. The relaxation of this excited electron leads to a cascading process, converting into energetic phonons. This ensemble of energetic phonons will down convert into a state of multiple thermalized electrons and phonons. This phenomenon leads to the formation of a resistive state, which is

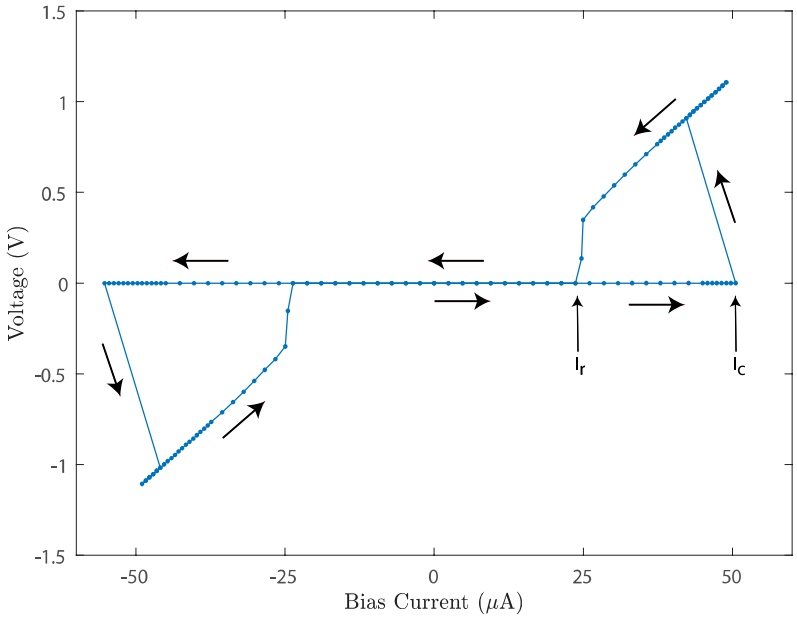


**Figure 1.1:** Example of an I-V curve in a superconducting nanowire. Image taken from a NbTiN nanowire. Larger arrows are used to indicate the direction of the ramping of the current, highlighting the hysteretic behavior of the curve

generally referred as hotspot. The hotspot pushes the current to flow on the sides of itself and if the current density exceeds the critical current density, a completely normal-state region is formed within the wire. This normal-state region produces a voltage pulse, whose height is then equal to the product between the current flowing in the wire and the resistance of the hotspot (generally, in the order of 10 kΩ). This pulse can be read using conventional electronics apparatus, such as oscilloscopes. As the current leaves the nanowire, the hotspot will cool down, resetting the detector with an exponential dynamic. The reset time is generally in the order of few ns up to hundreds of ns. Artistic schematic of the hotspot formation and pulse reading is shown in Figure 1.2.

Since, the size of the hotspot depends on the photon wavelength and the detection depends on the diameter of the generated hotspot, a cutoff in the detection wavelength is supposed to be inversely proportional to the width of the wire. This has been experimentally proved by Lusche et al. [13], this indicates that the wire width needs to be similar to the size of the hotspot generated upon photon absorption. This has pushed for years the fabrication techniques to pattern wires below 50 nm

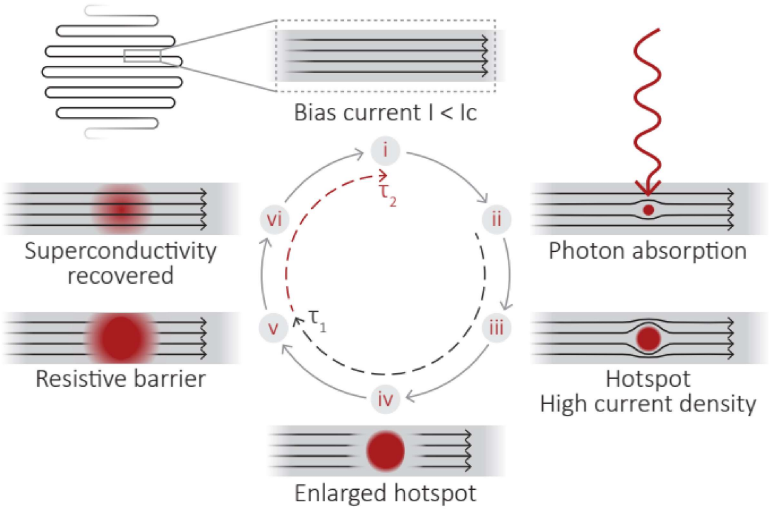


**Figure 1.2:** Artistic representation of hot-spot formation in superconducting nanowire. Image readapted from Natarajan et al., *Superconducting nanowire single-photon detectors: physics and applications* [12]. In this representation at time $\tau_1$ the pulse is generated by the bias current flowing through the resisitive barrier. Time $\tau_2$ is the recovery time, at the end of this cycle a new photon can be detected.

width [14] in order to increase the cut-off detection wavelength. In recent years, theoretical works suggested single-photon detection in micrometer-wide single photon detectors [15] and it was subsequently followed by multiple experimental verification [16, 17, 18]. Early models of photon detection were, thus, limited since they did not take into account vortex-assisted detection, while time-dependent Ginzburg-Landau models for photodetection proved that it can be mediated by the creation of vortex and anti-vortex pair. Applying kinetic-equation models for electron and phonon distributions, single photon sensitivity was predicted in micrometer-wide wires, [15]. Micrometer-scale features allow for fast high-yield production in photolithography-based foundry processes, enabling for large area single photon detectors, which are fundamental for low photon flux applications on wide areas, in particular deep-space and quantum communications, but also for dark matter detection [19] and high-energy physics. Not only using micron-wide-wire SNSPD (which are also referred as Superconducting Microwire Single Photon Detector, SMSPD) fabrication may lead to faster production, but, wide-wire single photon detectors allow a significant reduction of the kinetic inductance of the device, which in turns increases the maximum count rate and reduces the jitter time.

Unlike the other technology used in single photon detection, such as photomultiplier tubes (PMT), single photon avalanche photodiodes (SPADs) and Transition-Edge Sensor (TES), SNSPDs can combine high detection efficiency, high timing resolution, and low noise in the same detector design, at the expense of lower operating temperatures. In particular, the records for highest system detection efficiency (SDE), highest count rate, lowest dark count rate (DCR) and lowest jitter time, which is the uncertainty on the arrival time of the electrical pulse on the readout timing resolution are held by SNSPD. For SDE in 2020, D. V. Reddy et al. demonstrated a SNSPD with an efficiency of 98 % [20] and in 2021 J. Chang et al. reported a SDE of ($99.5\ ^{+0.5}_{-2.07}\%$) [21]. For jitter time, in 2020 B. Korzh et al. demonstrated single photon detection with 2.6 ps jitter time in visible region and 4.5 ps in 1550 wavelength [22]. The lowest dark counts were obtained by J. Chiles et al. with a DCR of $6 \times 10^{-6}$ counts/s [17]. In 2023, I. Craiciu et al. demonstrated an SNSPD with 1.5 Gcps count rate at 1550 nm wavelength [23]. A visual comparison of holding records for each figure of merit, measured at 1550 nm, is shown in Figure 1.3

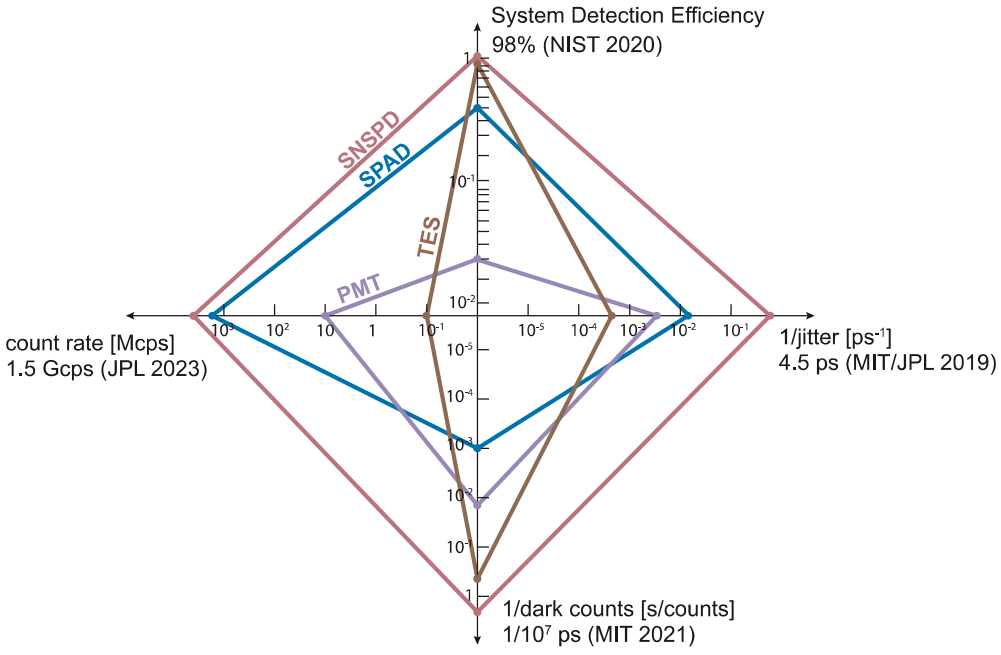


**Figure 1.3:** Comparison of main figures of merit, measured at 1550 nm wavelength, for SNSPD, photomultiplier tube (PMT), Transition-Edge Sensor (TES) and single-photon avalanche detector (SPADs)

However, realizing a single device having high performances in all these metrics

remains a significant challenge, since enhancing one of the metrics results in deterioration of one of the others. Not only these device have shown appealing properties in single-photon sensing, from UV (250 nm) [24] to infrared ($\geq$ 10 µm) [25], but lot of research has produced in the design and realization of novel techniques for pixel-level readout [26] and fabrication of large array of SNSPD array, reaching up to 400 kpixels array, with a footprint of 4 $\times$ 2.5 mm$^2$, with a spatial resolution of 5 $\times$ 5 µm [27].
SNs are not only a cutting-edge technology in the field of photonics, but they have emerged as a promising technology in digital electronics [28, 29], microwave technologies [30] and neuromorphic computing [31].

## 1.2 Thesis objective

Recalling the necessary requirement for hotspot creation, $E_{ph} > \Delta$ and rewriting the superconducting gap as $\Delta = 1.764\ k_B T_c$, according to Bardeen − Cooper − Schrieffer (BCS) theory, it is immediately possible to notice one big trade-off in SNSPDs technology. Since a higher $T_c$ is desired for operating the devices at higher temperatures, thus reducing the complexity and the cost of cooling equipment, on the other hand a lower $T_c$ guarantees a better sensitivity in mid-infrared regime. At this stage, state-of-the-art NbN and NbTiN allow for best performances in detection efficiency and time resolution when working at 2.2 K and above. In the last years, many advancements have been done in the field of optimization of SNSPDs, as the many records that this technology holds, but a clear correlation between normal-state properties and device performances has not been found yet. In 2021, Zolotov et al. showed a correlation in their data between the sheet resistance of the sputtered NbN films and the detection performances of fabricated results, showing a proportionality between the film property and the metric of the device [32]. This result has paved the way for the research in combining high $R_s$ and high $T_c$, opening the research in superconducting thin film material sputtering and post-processing techniques.
In this work, the optimization for high resistivity superconducting thin film processing is reported, involving magnetron sputtering deposition of NbTiN thin films, by sputtering $Nb_{0.5}Ti_{0.5}$ compound target in a nitrogen-rich atmosphere and fabrication technique based on maskless optical lithography. The usage of this target instead of the more common $Nb_{0.7}Ti_{0.3}$ has led to the sputtering of superconducting thin films with a $T_c$ of the films close to the the usual NbN, but with a higher resistivity. This

is expected to lead to better performances in final devices, in particular in larger plateau in the saturation of the photon count rate.

The e-beam lithography is a technique that was deeply optimized in the years for patterning superconducting nanowire, but it suffers from relatively low speed of patterning, which becomes more relevant when moving towards wafer-scale processing. Indeed generally some hours may be needed for properly patterning thin films, while with a maskless optical lithography equipment, such as Heidelberg MLA150, present in MIT.nano facilities, it is possible to expose a 100 mm wafer within 20 minutes. In addition to that, the processing proposed in this work for optical lithography do not require hazardous chemical handling, for example Tetramethylammonium Hydroxide (TMAH) which is required for development of Hydrogen silsesquioxane (HSQ), a negative-tone resist commonly used for high resolution patterning, below 18 nm. The main limitation of the tool is represented by the resolution limit, nominally 1 µm, this means that this do not represent an alternative to e-beam manufacturing for nanometer-scale fabrication, but thanks to recent experimental proof of single photon sensitivity in micron-wide-wire devices, maskless optical lithography is expected to play a significant role in large-area device fabrication for fast wafer-scale processing.

The order of the chapters in this work follows the suggested path for superconduting nanowire technology when working with new materials.

1. Thin film deposition and characterization
2. Fabrication techniques
3. Single wire and detector performances characterization

Following this order, the following thesis is organized as follows:

- **Chapter 2: Thin Film Sputtering and Characterization**. It is explained the process for magnetron sputtering and characterization setup for superconducting thin films. Later on, superconducting properties, as a function of deposition parameters are analyzed, in particular bias power and deposition pressure. Finally, the main optical properties, analyzed by Variable Angle Spectroscopy Ellipsometry, a technique that will be explained further, and the extraction of A and B parameters for thin superconducting films, whose

meaning is explained further as well.

- **Chapter 3: Fabrication technology of superconducting microwire single photon detectors**. It will be explained the fabrication steps for superconducting-nanowire technology, involving maskless optical lithography. The optimization of optical lithography and reactive ion etching (RIE) process for micron and sub-micron scale patterning will be proposed for complete and reliable photoresist removal.

- **Chapter 4: Photon-detection and electrical characterization of superconducting microwire**. The experimental setups, involving mainly cryostats working below liquid-helium temperature and apparatus description for dip-stick probe in liquid-helium dewars, for characterization at 4.2 K. Then main results for photon-detection and electrical characterization of NbTiN based microwires are proposed showing the first NbTiN-based SNSPD realized in the group, but whose count rate does not present saturation in internal detection efficiency.

- **Chapter 5: Conclusion and future outlooks**. A summary of the results reached in this work are proposed. Possible future material deposition techniques and strategies are proposed for improvement of NbTiN thin films. Characterization techniques will be proposed to analyze the effects of deposition parameters at atomic scale.

# Chapter 2

# Thin Film Sputtering and Characterization

The NbTiN films were prepared by RF magnetron sputtering technique using AJA International ATC Orion Sputtering System. The magnetron sputtering technique differs from traditional sputtering by the usage of magnets, which force, through a magnetic field, the $Ar^+$ ions on a longer path (spiral instead of straight lines), thus increasing the ionization rate in the deposition chamber, which results in an increase of the deposition rate at lower Ar pressure. In this work, the target used was a $Nb_{0.5}Ti_{0.5}$ target, sputtered in a nitrogen rich atmosphere, thus the bombarded Nb and Ti will react with the nitrogen injected in the chamber and then deposit on the desired substrate.

Each deposition is made of six consecutive steps:

- **Spark of the plasma**. The power is increased gradually until a fixed set-point, which is necessary to completely spark the plasma. This appears as a bump in the voltage between the cathode and the anode and by the appearance of typical bright color of plasma inside the deposition chamber. In this step the pressure is set to a high level to facilitate the sparking, generally around 40 mTorr, which is much higher than the pressure used during the sputtering of the target. In this stage only Ar is injected in the main chamber.

- **Lowering of the pressure**. Once the plasma is correctly sparked and stable, the chamber pressure is lowered to the operating pressure, generally between 2 and 4 mTorr, depending on the sputtered material and the desired deposition

rate. The Ar flow is kept constant for 2 minutes, in order to have a uniformity of the plasma inside the chamber.

- **Introduction of active gas**. In this stage the conditions of the previous step are kept constant, but the active gas is injected and the flow is kept constant for 3 minutes, in order to have a uniform gas distribution before proceeding with the next steps.

- **Power ramp-up**. Now that the pressure of the chamber and the gas are uniformly distributed in the chamber, the RF power is gradually ramped up to the nominal value for the sputtering. Once power is arrived at set-point, the power is kept constant for 2 minutes, this is performed to both stabilize the plasma at the RF power set-point and to sputter the superficial layer of the target, in order to sputter a target as pure as possible.

- **Sputtering**. At this stage the shutter covering the target is opened letting the sputtered material go towards the sample. The time for the shutter open is defined according to the desired thickness.

- **Shut-off of the system**. The shutter is now closed, power is gradually set back to zero and pressure is set to non-sputtering conditions.

The tool used throughout this work belongs uniquely to our group and whose use is uniquely dedicated to depositions of superconducting films (mostly NbN and MoSi), in order to avoid contamination with other materials. The system is made of a main sputtering chamber and a load lock, which is used to load and unload the samples, without venting the main chamber, allowing for extremely low pre-sputtering pressure (between 5 $\times 10^{-9}$ and 1 $\times 10^{-8}$ mTorr), thus limiting the contamination of the films from external impurities.

## 2.1 Measurement setup

In the following sections the description of the setup, equipment and methodology for measurement of sheet resistance, $R_s$, critical temperature, $T_c$ and thickness, $d$ will be

explained. For these measurements three different equipment are needed: a room-temperature 4-probe multimeter, a dedicated dip probe for cryogenic measurement of the critical temperature and an ellipsometer setup.

### 2.1.1 Sheet resistance

The sheet resistance of thin films is measured using a 4-probe setup, this configuration allows to remove the contact and wire resistance, which would affect the measurement.
A correct measurement consists of two measurements, differing from each other by the rotation of the sample by 90 degrees, after collection of the two values, namely, R1 and R2, it is possible to evaluate the sheet resistance of the films through the following formula:

$$R_s = c\,\frac{\pi}{\ln(2)} R. \tag{2.1}$$

In the formula, $R$ is the average between the two measured resistance R1 and R2 and $c$ is a correction factor which depends on the geometry and shape of the sample, for infinitely large rectangular films it is equal to 1. From the sheet resistance it is possible to evaluate the resistivity, $\rho$, of the film as it follows:

$$\rho = R_s\, d \tag{2.2}$$

In the formula, $d$ is the thickness of the film.

### 2.1.2 Critical temperature

In order to evaluate the critical temperature it is necessary to measure the resistance of the film as a function of the temperature. For this task, a dedicated dip probe was used, which allows for fast evaluation of R(T) curves of two sample dies at the same time. The probe is made of two printed circuits boards (PCBs), which, during operations are placed one on top of the other. The sample die is placed on the bottom one on region plated with electroless nickel immersion gold, with a diode-based temperature sensor. On the top PCB four pogo-pins per each chip are placed, in order to both measure the resistance using a four-probe technique, as explained in Section 2.1.1 and to hold the chip during the measurement. The four pogo-pins are

then connected to the lower PCB, through a connector and the four signals for each chip are then sent to an external multimeter, through a feedthrough, to measure the resistance. The measurement is run using a Python code, which allows for setting the multimeter on 4-wire setup and sampling the resistance once each second for both mounted dies. The current is set to 100 µA to avoid self-heating phenomenon and guarantee a low uncertainty on the measurement. While the measurement runs, the operator has to lower the probe down into the dewar in order to cool down the chips, or raise it up for warming it up. On both directions, the speed is generally low in order to cool down and warm up properly the chip avoiding big jumps in temperature. The temperature decreases by lowering the probe down into the dewar until liquid helium is reached, thus reaching 4.2 K temperature. Then, this tool do not allow for critical temperature measurement of very low-$T_c$ materials, such as thin MoSi or WSi, but it is perfectly suited for NbN, NbTiN and high-$T_c$ materials such as $MgB_2$ or Yttrium Barium Copper Oxide (YBCO).

### 2.1.3 Thickness and optical constants

The measurements of the thickness of the films and optical constants (refractive index, $n$, and extinction coefficient, $k$) were realized using an ellipsometer setup, in particular the tool is SE2000 from Semilab. The complete description of the working mechanism of an ellipsometer and the meaning of the parameters is explained in the Appendix in Chapter A.1. The working mechanism description is limited to our tool and brief explanation of main analysis parameters, such as $\Psi$ and $\Delta$, is provided but it is not meant to be a complete guide on ellipsometry.

Since this mechanism relies on optical properties of the film it is necessary that all the contaminating particles are removed and, since the ellipsometer was in MIT.nano facilities and the sputtering system is outside of it, the contamination is almost inevitable during the transportation from the chamber to the characterization tool. For this reason, prior to any measurement the samples are cleaned in a non-destructing way, by sonication for 3 minutes in acetone and 3 minutes in IPA and dried with a $N_2$ gun.

The first step is the measurement of $\Psi$ and $\Delta$ values, as a function of the impinging wavelength, which are measured in the visible and near infrared (NIR) spectrum of the electromagnetic radiation, from 240 nm up to 1700 nm. This measurement is repeated for different angles in particular 45, 50, 55, 60, 65, 70 and 75 degrees, this

is made to create a unique data set. For this reason, this method is called Variable Angle Spectral Ellipsometer (VASE). The measurement of $\Psi$ and $\Delta$ is considered as exact (within the uncertainty of the tool). On the other hand, ellipsometry is an indirect method, this means that the measured $\Psi$ and $\Delta$ data cannot be converted directly into thin film optical properties, but an analysis model is necessary. The necessity of a model for fitting the experimental data is the major weakness of this technique and the one which is responsible for uncertainty or errors in the measurements. In addition to that, since this technique is unique, the (reasonable) values which best fit the experimental data, by least-square minimization, are considered as exact. Then, the most important part in ellipsometry analysis consists of finding the proper model for fitting the experimental data to get the optical constants and thickness of the films. The first step was a literature check for understanding the best model for fitting experimental data from ultra-thin absorbing films. Indeed, the ability of the superconducting films of absorbing the radiation in all the used spectrum and extremely low thickness of the films makes this choice fundamental. In Lucy Elizabeth Archer's thesis, [33], which is focused on studying optical properties of thin films of NbN using the same experimental setup, the model chosen is the Drude model, which generally used for absorbing material in NIR and visible range, with it the Lorentz model was used. These two analysis models were used in combination with a third model, called *IR Tail*, used simultaneously to fit at best the data (this last is not present in the work of Lucy Elizabeth Archer, probably because it is a recent upgrade and it was observed to result in a better fitting of the data).

The first part of the simulation consists of providing a structure to the software, in particular a Si wafer as a substrate, on top of it a 300 or 100 nm thick $SiO_2$ layer (a good approximation for the thickness of the oxide layer was measured with an ellipsometer setup before sputtering the films, in order to have a reference for future measurements) and NbTiN layer, whose thickness, $n$ and $k$ parameters are unknown. From an initial guess of the thickness of NbTiN film, generally around 5 nm, the software automatically tries to fit the experimental data with the parameters of the model ($E_\mathrm{p}$ and $E_\Gamma$ for the Drude model, $f$, $E_0$ and $\Gamma$ for Lorentz model and $A$ for the IR Tail model).

From the fitting of the ellipsometer data, in particular $E_\mathrm{p}$ and $E_\Gamma$, it is also possible to recover some useful normal-state parameters, such as the conductivity, $\sigma$ or

equivalently the resistivity, $\rho$ and $R_s$ of the superconducting thin film, following the equations:

$$\sigma = \frac{\varepsilon_0 E_{\mathrm{p}}^2}{E_\Gamma \hbar}, \tag{2.3}$$

$$\rho = \frac{1}{\sigma} = \frac{E_\Gamma \hbar}{\varepsilon_0 E_{\mathrm{p}}^2}. \tag{2.4}$$

At the end of the fitting, if the measurement of the oxide layer is sufficiently close to the one measured in our own ellipsometer setup (generally within 1 nm) and if the electrical parameters estimated by the measurement are sufficiently close to the values measured with the 4-probe setup, the measurement is considered correct.

## 2.2 Target poisoning

The sputtering power is generally limited by two main factors: plasma stability and poisoning of the target. The first one is due to the formation of too energetic plasma, this can be noticed since the plasma starts to be unstable, turning on and off continuously. The second one, poisoning of the target, appears when the plasma power is so high that not only we sputter the $Nb_{0.5}Ti_{0.5}$ target, but also the already deposited superconducting films. The minimum power for poisoning can be found through a jump in the RF voltage as a function of the power injected into the target, since the trend of voltage versus power is generally linear. For this task, a linear sweep of the power was performed to monitor the variation of RF voltage with respect to the power provided by dedicated RF gun. Generally, the power is set to the maximum power that guarantees stability of the plasma and avoid target poisoning. In our tests, no target poisoning was observed, but starting from a RF power of 120 W the plasma started to become unstable. For this reason to guarantee a constantly stable plasma and no target poisoning a RF power of 100 W was set throughout this work.

## 2.3 Results

The normal state and superconducting state properties strongly depend on the sputtering conditions in the chamber, among all, chamber pressure, $N_2$ and Ar flows, substrate temperature, RF power, bias and many others but also on the substrate material, for example $SiO_2$, $SiN_x$, Si, MgO or even 2D materials [34]. MgO substrates are generally used with NbN, since MgO provides the best lattice matching with NbN, leading to an increase of critical temperature. In this work only $SiO_2$ on Si substrates were used, since it is was shown that it guarantees the best device-level performances, if compared to the other Si-based substrates [34] and this material is widely used in photonics integrated circuits for quantum applications. In Section 2.2 the maximum power which safely allows to work without plasma instability and target poisoning is around 100 W, this power will be used for all the depositions.

### 2.3.1 Non bias-assisted sputtering

It was shown, using the same magnetron sputtering system of this thesis, by Dane et al. that by applying a bias during the sputtering of NbN, substantial changes appear, above all an increase of the critical temperature and the lowering of the resistivity of the sputtered NbN films [35], showing an optimal point for critical temperature using a $N_2$ flow of 6 sccm. The $N_2$ flow has been shown to strongly change the properties of the sputtered films, generally showing a dome-shaped curve in the critical temperature with respect to the nitrogen content. A similar study has been recently published by Pratiksha Pratap et al. by studying epitaxial growth of NbTiN on MgO substrates and the different superconducting and physical properties of the films depending on the $N_2$ flow [36]. The usage of the bias is extremely useful because it allows for increase of the critical temperature without requiring an increase of substrate temperature, which can be useful for deposition on temperature-sensitive material, such as polymers, and at the same time it does not require long cooling time of the chip carriers. Firstly, the sputtering time was left unchanged for all the samples and equal to 300 seconds, in this way it was possible to evaluate a starting point for the critical temperature and resistivity of the films.

In Figure 2.1, the sheet resistance and the critical temperature was shown, it is possible to notice that increasing the nitrogen flow the sheet resistance increases, this is due to the fact that the resistivity is expected to increase as the nitrogen flow

increases, since the more nitrogen is inflated in the chamber the more interstitial N atoms are expected to be present, thus the films tend to be less-metallic. It is noticeable to mention that also 9, 10, 12 and 15 sccm were tried as nitrogen flow, but all of them did not show superconducting transition before 4.2 K (9 sccm reached the half of the transition in R(T) but zero-resistance was not verified). From these values it can be noticed that the sheet resistance of these films is promising, since it is possible to get values higher than 1 kΩ/sq. On the other hand, the critical temperature for the films are not optimal, if compared to other groups' results, in which it was shown results of highly-resistive thin films, but with critical temperature around 8 K, such as recent results of Zolotov et al. [37], in which they sputtered NbN using very large flow of $N_2$, but to keep sufficiently high the critical temperature they sputtered on a heated substrate, 300 °C and using a bias. Using the ellipsometry the thicknesses of the films were evaluated, and thus the deposition rate, showing generally a plateau in deposition rates for $N_2$ flow higher than 5.5 sccm saturating to a rate below 1 nm/min, Figure 2.2.

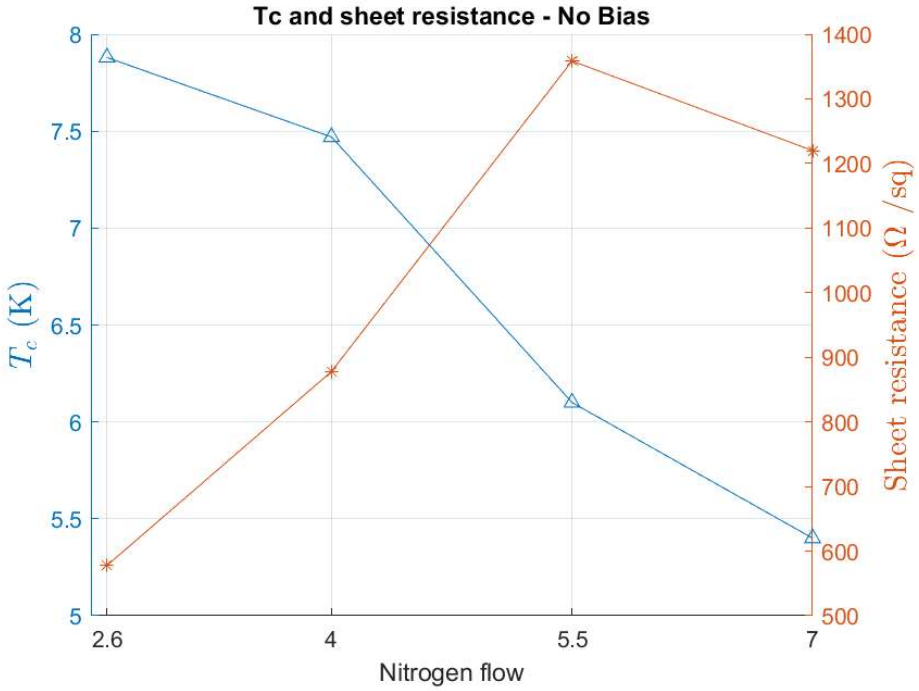


**Figure 2.1:** Sheet resistance and critical temperature for NbTiN thin films with 0 W bias. In this case films were grown using same deposition time and not same thickness, thus they do not result is same thickness. Nitrogen flow $\geq$ 9 sccm are not shown since $T_c < 4.2$ K

The lowering of the critical temperature as the nitrogen flow increases was also

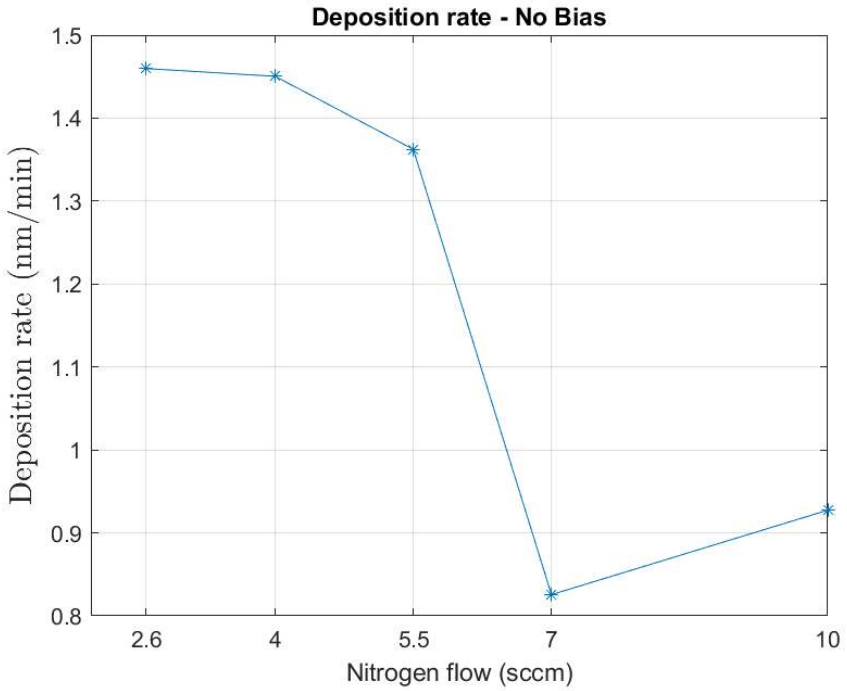


**Figure 2.2:** Deposition rate for non-bias assisted films, showing an abrupt drop in correspondence of 7 sccm of $N_2$

verified by Pratiksha Pratap et al, [36], confirming the dependence of the critical temperature with nitrogen content for non-bias-assisted NbTiN films. In particular they obtained an optimum for $T_c$ in correspondence of a $N_2$ partial pressure equal to 7 %, that using 40 sccm of Ar corresponds to 3 sccm of $N_2$. This may result in an optimum for simple $T_c$, but it would imply a low resistance. For this reason, alternative techniques were investigated for reaching sufficiently high $T_c$ without sacrificing the resistivity and this will be the subject of the following chapters. Since, it was possible to observe that the voltage in the chamber in not affected by the $N_2$ flow, the ionization rate is not expected to change significantly, thus the large drop in the deposition rate is suggested to be caused by a lower reaction rate between the active gas and the sputtered Nb and Ti, this may also lead to less cristallographic order, affecting the final microscopic properties of the films. This is expected to be the cause for the very low $T_c$ for nitrogen-rich films, then in the future chapters the bias will be used to allow for higher nitrogen flows without sacrificing the resistivity of the film.

### 2.3.2 Effect of bias and pressure

In the work of Dane et al. [35] it was demonstrated an increase of $T_c$ by using a 50 W bias during the sputtering, but this also resulted in lowering the resistivity of the films. Thus, the effect of the bias on $T_c$ and $R_s$ was studied, trying to find an optimum bias power in order to limit the reduction of the resistivity, but still resulting in an increase of the critical temperature. Thus, a second experiment was performed keeping fixed the nitrogen flow, in particular 7-nm-thick films were sputtered injecting 7 sccm of $N_2$ flow and 26.5 sccm of Ar. The bias was swept between 0 and 50 W in a 2.5 mTorr sputtering pressure, results are shown in Figure 2.3. It was noticed that the $T_c$ is dependent on bias applied showing a proportionality between the two. On the other hand, the sputtered films, also for low bias, underwent a large decrease in resistivity (close to 40 %). In addition to the sweep of the bias, the effect of the pressure was observed. For this experiment three couples of samples were sputtered using 2.5 and 3 mTorr sputtering pressure, the samples were sputtered using the same deposition time, which resulted in comparable thicknesses (difference lower than 0.5 nm were measured with VASE technique), thus the samples can be safely compared. Results are shown in Figure 2.4. The resulting critical temperature was increased by a significant amount by lowering down the pressure down to 2.5 mTorr instead of 3 mTorr. Using 26.5 sccm of Ar and 4, 7 and 9 sccm as $N_2$ flows, which were used as a reference for low-, medium- and high-nitrogen flow, showing an increase of about 0.5 K for 7 and 9 sccm $N_2$ flow. At the same time, the change of pressure is not responsible for major differences in thickness. This could be resulting from a higher crystalline order in the material, induced by lower pressure leading to a more uniform arrangement of nitrogen atoms in the film.

Using a 9 sccm of $N_2$ flow a large resistivity, 416 μΩ cm, was observed, which represents an increase of about 100 μΩ cm with respect to 7 sccm $N_2$ flow, but at the same time the film was featured with a high critical temperature for a 8-nm-thick film. To provide a comparison to this result, the resulting film shows a critical temperature close to the optimized-bias-sputtered NbN for the same thickness, but at the same time a higher resistivity was observed. The resistivity can be compared to the results obtained in the group for nitrogen-rich NbN for wide wire single photon detectors, 390 μΩ cm [38].

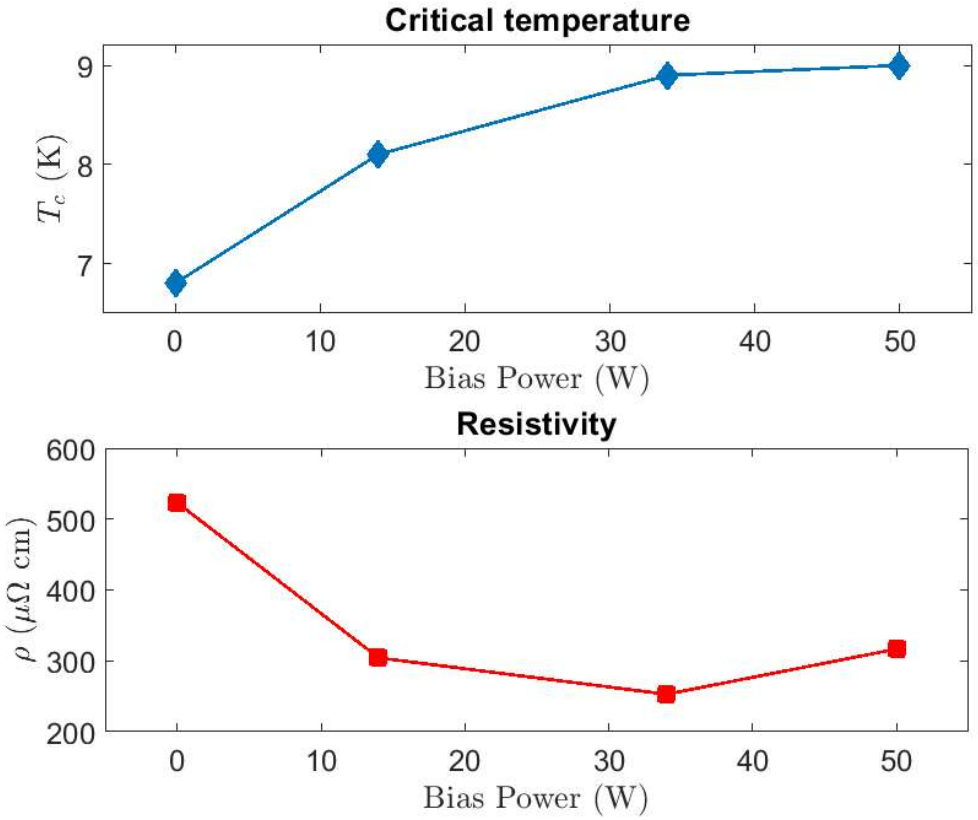


**Figure 2.3:** Effect of the bias on superconducting properties of magnetron sputtered 7-nm-thick NbTiN films. The films were sputtered all in the same conditions, by only sweeping the bias. **Top**: Effect of the bias on $T_c$. **Bottom**: Effect of the bias on the resistivity

### 2.3.3 Optimization of bias-assisted sputtering

For non-bias assisted deposition for a nitrogen flow below 9 sccm, 5-nm-thick films still show a superconducting transition above liquid helium temperature in absence of an additional bias, for higher nitrogen content the transition temperature was still below the liquid helium temperature. On the other hand, these films were the most interesting since they are featured with the highest resistivity, due to the large concentration of interstitial nitrogen.

From the good results on optimization of critical temperature by lowering the sputtering pressure and using 50 W bias power, the effect of nitrogen content was studied by keeping a 50 W bias and a sputtering pressure of 2.5 mTorr, with an Ar flow of 26.5 sccm. As a first attempt, the sputtering process were performed using the

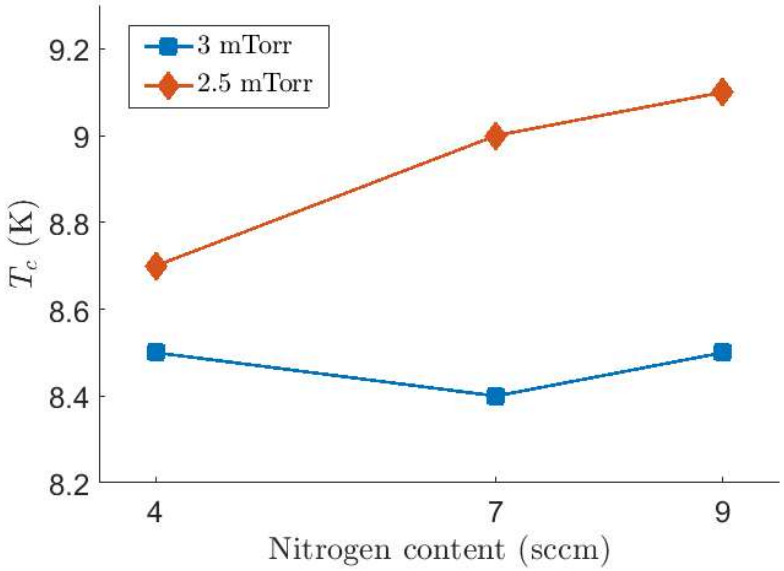


**Figure 2.4:** Effect of the sputtering pressure on critical temperature for three different nitrogen content. For each couple of samples the deposition time is equal in order to ensure equal thickness.

same sputtering time, 4 minutes, using 4, 5.5, 7, 8.5, 10 and 11.5 sccm of $N_2$. From this first set of films it was possible to extract the effect of the different nitrogen concentrations on resistivity and deposition rate of the films. The corresponding results are shown in Figure 2.5 and 2.6.

According to experimental values, the resistivity of the film show a linear dependency with the nitrogen flow, the fitting parameters can be extracted and it is shown that the resistivity follows the equation:

$$\rho = 29.7\ \mathrm{N_2\ flow} + 188.7 \tag{2.5}$$

In the equation $\rho$ is measured in $\mu\Omega\,\mathrm{cm}$, while the $N_2$ flow in sccm. As contrary of the resistivity, an inverse proportionality between the deposition rate and the nitrogen flow can be observed. Thus, the higher the nitrogen content the lower the deposition rate. This result is very similar to results obtained with NbN, where the deposition rate is between 3 and 6 nm/min, and in correspondence of the optimum for critical temperature it is around 4 nm/min. This trend can be caused by an increasing reaction time of the active gas with the sputtered Nb and Ti, this linear

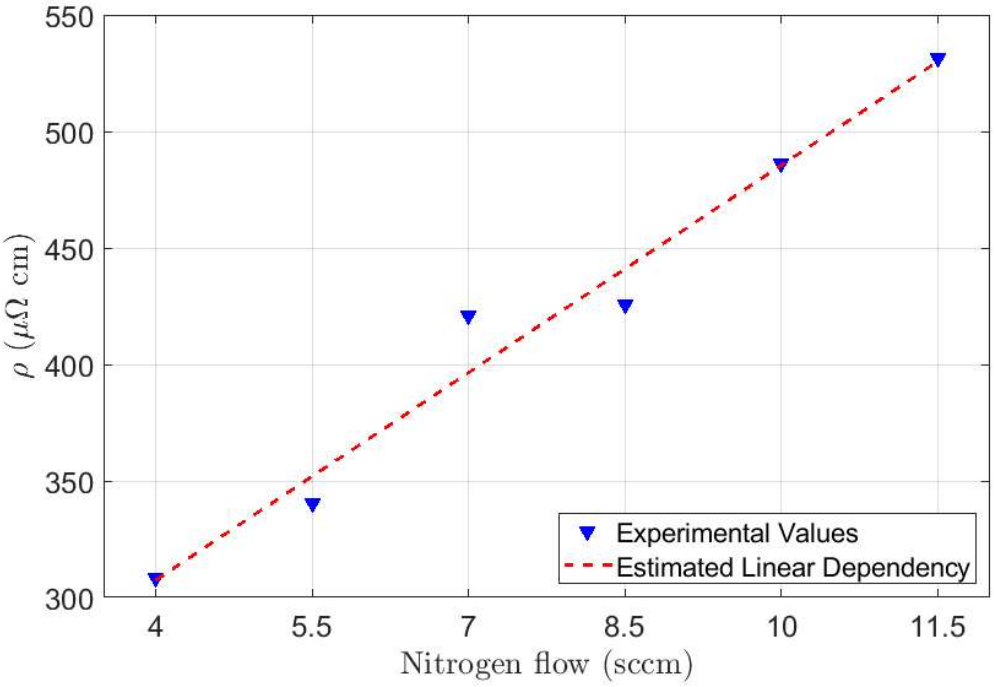


**Figure 2.5:** Resistivity of sputtered films, deposited using 2.5 mTorr deposition pressure

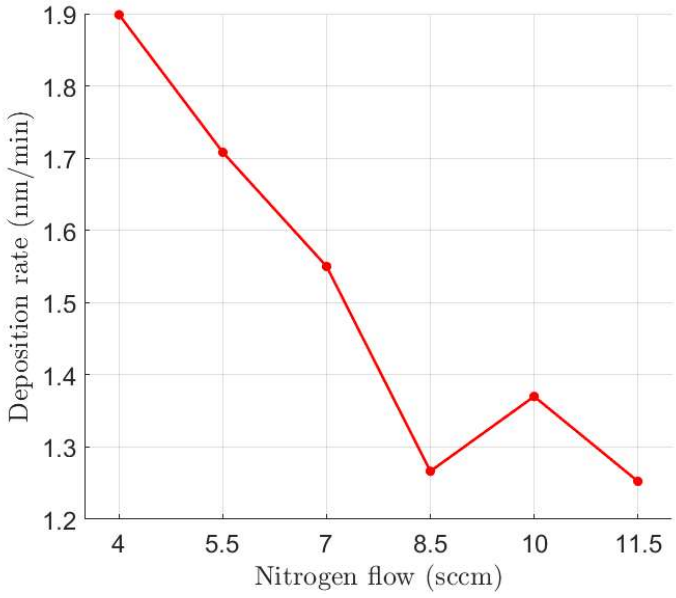


**Figure 2.6:** Deposition rate versus nitrogen flow

regime suggests that the additional bias during the deposition favors the reaction of the nitrogen, thus not resulting in big jumps in the deposition rate. Secondly,

once the sputtering rate is known, the deposition times were tuned accordingly, to sputter for each of the nitrogen flow one 5-nm-thick film. This was further verified by ellipsometry measurement, showing that each of the films were within 0.2 nm of error with respect the nominal 5 nm thickness (the thinnest was 4.8 nm while the thickest was 5.2 nm), this difference is generally in the same order of magnitude of uncertainty of the tool and it is not expected to play a significant role. R(T) curves for different $N_2$ flows are shown in Figure 2.7.

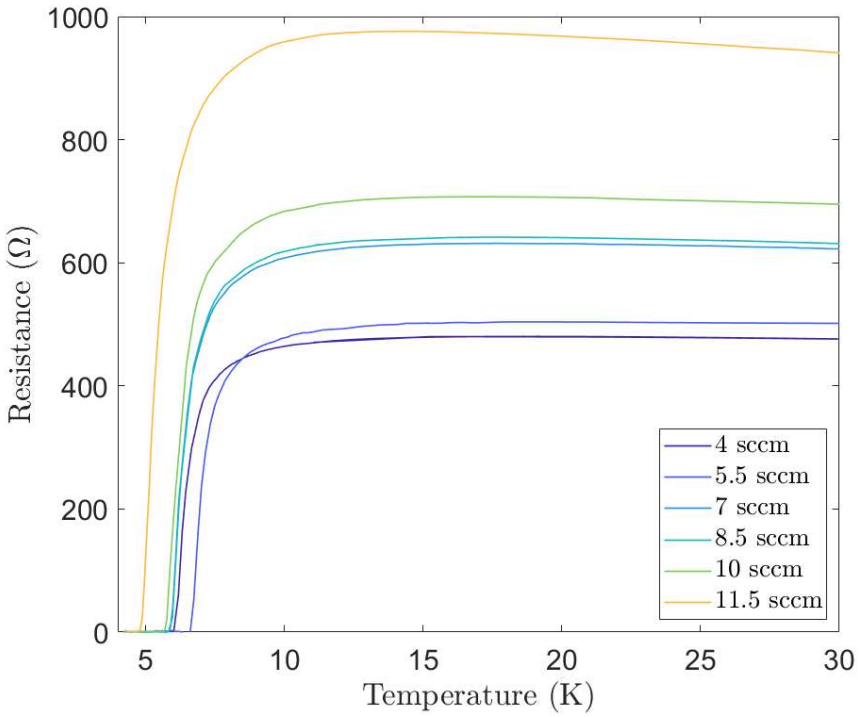


**Figure 2.7:** R(T) of superconducting thin film as a function of nitrogen content in the chamber

It is possible to observe that higher-$N_2$ films are more resistive (or less metallic) than $N_2$ poor films. The resulting $T_c$ are shown in Figure 2.8. It is possible to observe a maximum of critical temperature in correspondence of 5.5 sccm nitrogen flow, corresponding to a value of 7 K. It is worth to be mentioned that this result is very close to the one obtained for NbN, where the maximum point was measured with 6 sccm. In that case the $T_c$ of the resulting film was equal to 7.8 K, thus resulting in a film with a $T_c$ 0.8 K higher. It is also possible to observe a central flat region around the optimum point and then an abrupt drop of $T_c$ for $N_2$ flow larger

than 10 sccm. Since, for high-efficiency SNSPDs both a high resistivity and a high critical temperature are recommended, a general parameter that can be taken into account is the product $\rho T_c(N_2)$, Figure 2.9. The resulting curve $\rho T_c(N_2)$, show a dome-shaped curve with a maximum in correspondence of 10 sccm of $N_2$ flow and its value is strongly affected by the $N_2$ content showing an increase of 51 % from 4 sccm to 10 sccm. This suggests that the different $N_2$ content in the film is responsible for significant variation in the film properties.

To provide a fair comparison between the two materials, the values for $\rho$ and $T_c$ were extracted from Dane et al. work [35] and the product $\rho T_c$ is compared as a function of the $N_2$ content, with the results in this work. The results are shown in Figure 2.10. It is possible to notice that the product $\rho T_c$ is generally higher in NbTiN, with respect to both the two NbN film sets. All the films have a thickness of 5 nm and the results are cropped in order to be in the same range of $N_2$ flow.

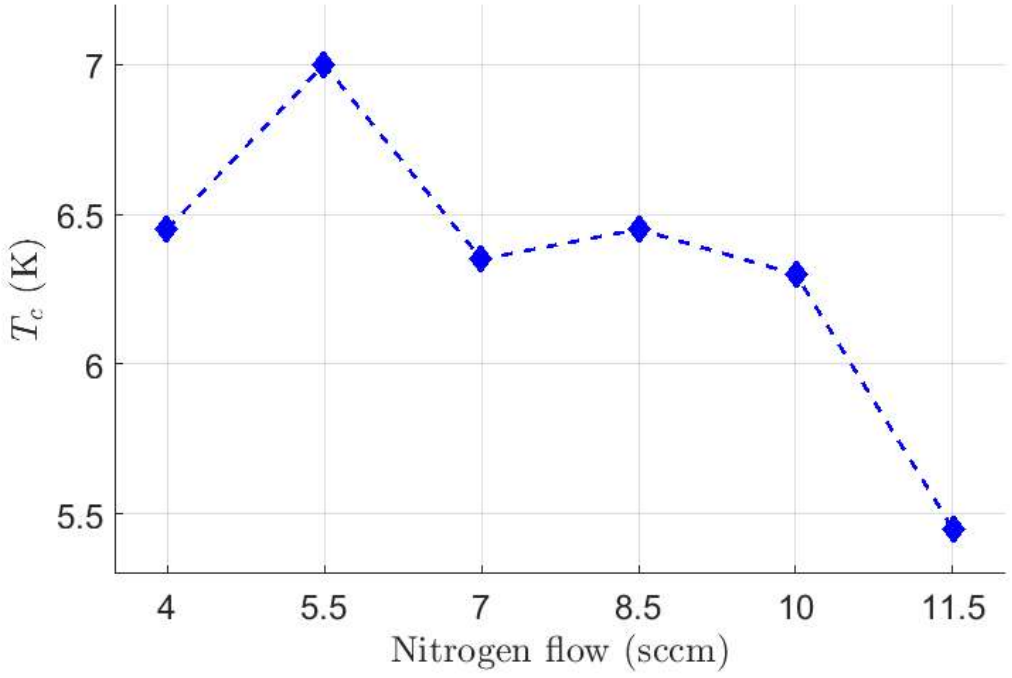


**Figure 2.8:** $T_c$ dependence on nitrogen conten for 5-nm-thick NbTiN films, showing an optimum in correspondence of 5.5 sccm $N_2$ flow.

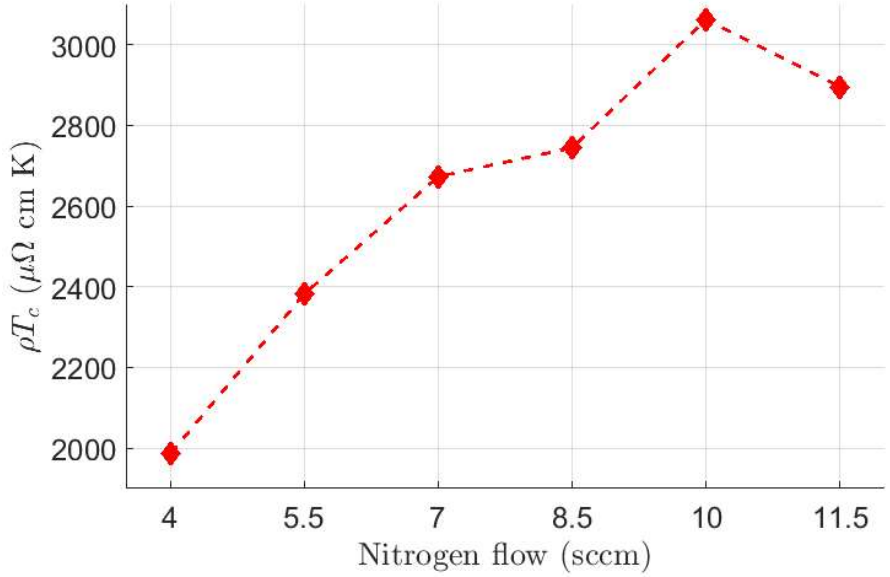


**Figure 2.9:** $\rho T_c$ product as a function of nitrogen flow evaluated for a set of 5-nm-thick NbTiN thin films.

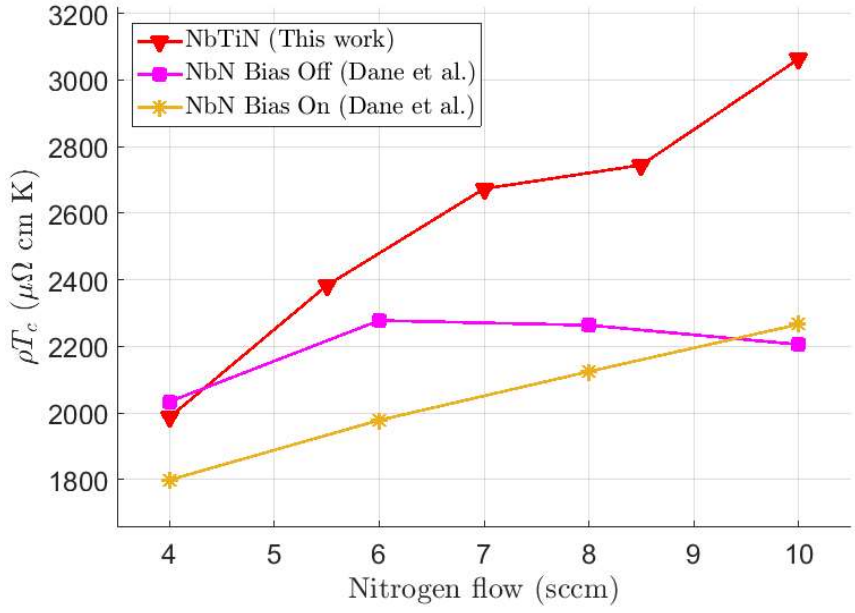


**Figure 2.10:** Comparison of the figure of merit $\rho T_c$ as function of different $N_2$ content between NbN and NbTiN. All the films have a thickness of 5 nm and were sputtered with the same sputtering system.

## 2.4 Dataset analysis

From the dataset collected for NbTiN thin film deposition, it was possible to observe some main correlations between the superconducting thin films metrics. First of all, as a main interest the correlation between the sheet resistance and the critical temperature, which are the two of the most important parameters when working with SNSPDs. For conventional metallic superconductor the critical temperature results to be independent from the sheet resistance, this has demonstrated to be false in NbN, [32] and in many superconductors used for SNSPD fabrication. Result can be shown in Figure 2.11

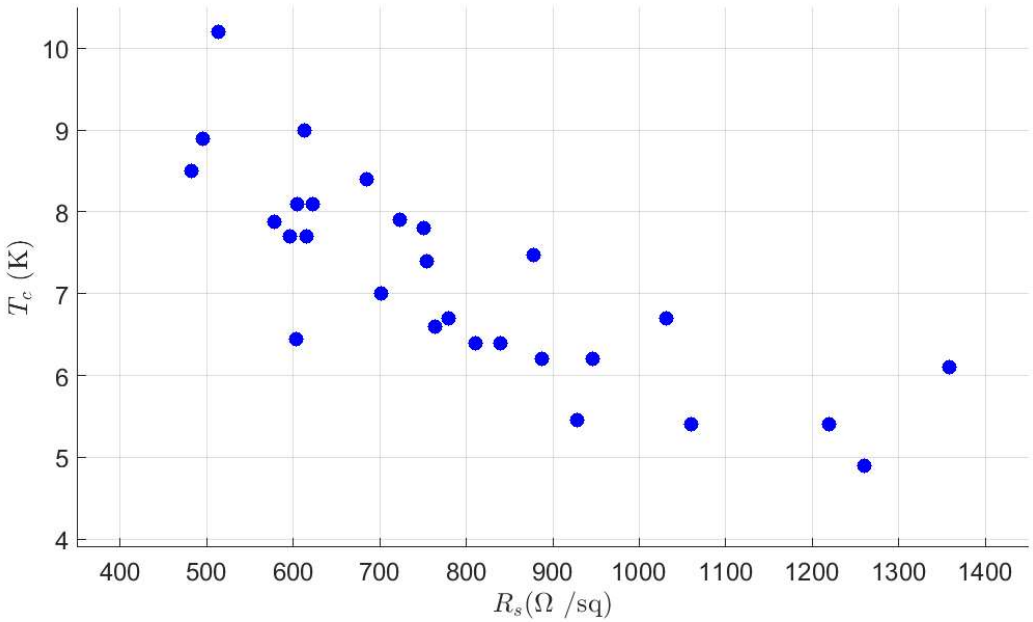


**Figure 2.11:** Dataset collection (35 samples) for relation between sheet resistance and critical temperature in NbTiN sputtered from $Nb_{0.5}Ti_{0.5}$ target

From this result it is possible to observe one of the main limitation in performances for SNSPDs: for high-performance devices a higher sheet resistance is desired, but as the sheet resistance increases the critical temperature decreases, thus limiting the working temperature for final devices. Some similar results have been obtained in the study of NbN by previous members of the group, which were studied and published by Y. Ivry et al. [39]. Also in this case, the scatter in the graph is too large to allow a confident fitting to any model for $T_c(R_s)$. As in the study of Ivry, the possible origin for this scattering of the data is the low quality of the grown films, in terms of cristallinity and strain, induced by the lattice mismatch with the

substrate. Indeed, in order to enhance the cristallinity order and the minimize the strain induced by lattice mismatch with the substrate, Y. Ivry et al. deposited NbN on heated MgO substrates (800 °C), instead of Si or $SiO_x$, since MgO shows minimal lattice mismatch with NbN.

Y. Ivry et al. observed that the parameters $d$, $R_s$ and $T_c$ do not have a scaling method between each other (i.e. $R_s(d)$, $T_c(R_s)$ and other combinations), then, known the suppression of $T_c$ with reduced thickness $d$ and increased disorder (or increasing $R_s$) the scaling of the product $dT_c$ as a function of $R_s$ was observed for a wide set of different superconducting ($\sim$ 30) thin film materials showing a clear trend in the function $dT_c(R_s)$ [39]. The relation was demonstrated to be:

$$dT_c = AR_s^{-B}. \tag{2.6}$$

From this equation $A$ and $B$ are fitting parameters. From observation that $B$ is generally very close to 1 and given $\rho \equiv dR_s$, then the Equation (2.6) can also be rewritten in a reduced form:

$$\frac{\rho}{R_s}T_c = AR_s^{-B} \Longrightarrow \rho T_c \sim \text{constant}. \tag{2.7}$$

It was further demonstrated that a trend between the parameters $A$ and $B$, implying that they may be determined by the granularity of the thin film. In this work, data were collected and $A$ and $B$ parameters were extracted, using MATLAB software resources, resulting in $A = 3.5 \times 10^4$ and $B = 1.03$. The fitting function is plotted with the measured data in Figure 2.12. These results were then added to the results of Ivry in Figure 2.12, showing that NbTiN is added among all the other studied superconductors, Figure 2.13.

It is possible to notice that some of the points do not match correctly the fitting function, this effect can be due either due to the lattice mismatch with the film, which may alter the cristallinity order or presence of some impurities may be responsible for that. Beside the presence of some points, mostly present on left-hand side of the graph (low $R_s$), it is possible to notice that for high $R_s$ the fitting improves, despite all the different sputtering conditions (mainly pressure, bias and nitrogen flow). In Chapter 2.3.3 it is demonstrated that the product $\rho T_c$ is altered and strongly in-

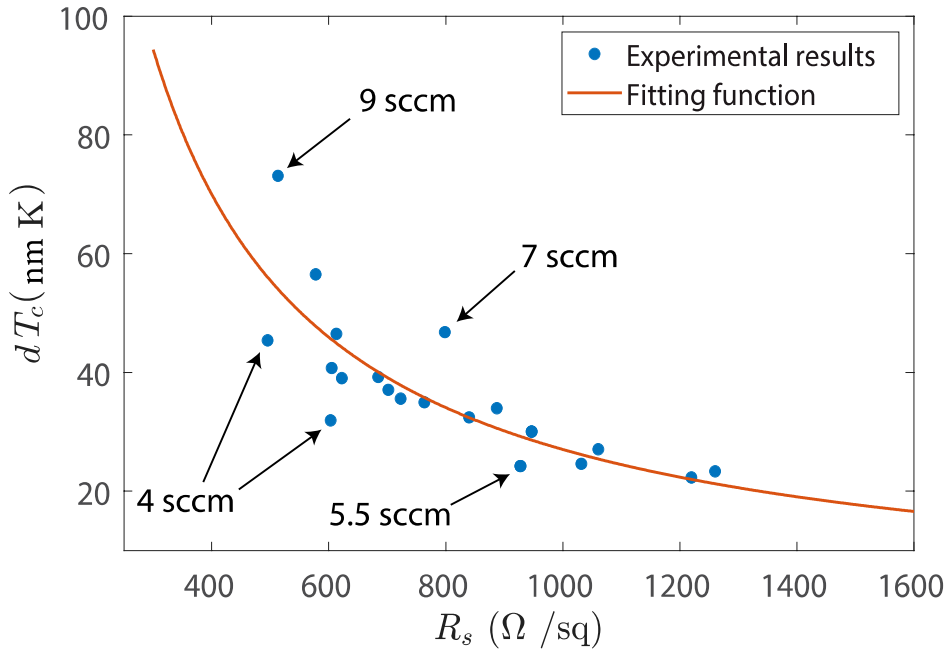


**Figure 2.12:** Experimental results for $dT_c(R_s)$ for sputtered NbTiN. Most of the point represent films grown in different sputtering conditions, specifically pressure, bias power and $N_2$ content. It is highlighted how the two major off-points sputtered using 50 W in 2.5 mTorr working pressure lays below the fitting function are sputtered with lower $N_2$ flow, while the two major off-points above the fitting curve are the one sputtered with higher $N_2$ flow

fluenced by the nitrogen content in the film. In order to have a better picture of the film properties more films are suggested to be sputtered in low $R_s$ regime ($\leq$ 400 $\Omega$/square down to around 100 $\Omega$/square), in order to have a clear picture if the the off-points are due to stochastic variations of the films or if there is a relation between film properties and the parameters $A$ and $B$. Thus, further experiments should be performed to verify a dependence between the fitting parameters of A and B and $N_2$ content in the resulting film, since it is possible to notice that especially in low-$R_s$ range the dispersion of the points becomes more relevant. In particular, if only bias-assisted sputtered NbTiN are taken into account, high-$N_2$ content films lies over the fitting function, while the low $N_2$ points are more favorable to sit below the fitting function. This suggests a dependence of $A$ and $B$ parameters with $N_2$. Since it was also observed that higher A values are obtained for high granularity of the films, which for NbTiN might be caused by the additional interstitial N atoms. This may agree with the results obtained in Chapter 2.3.3 for the product $\rho T_c$, which

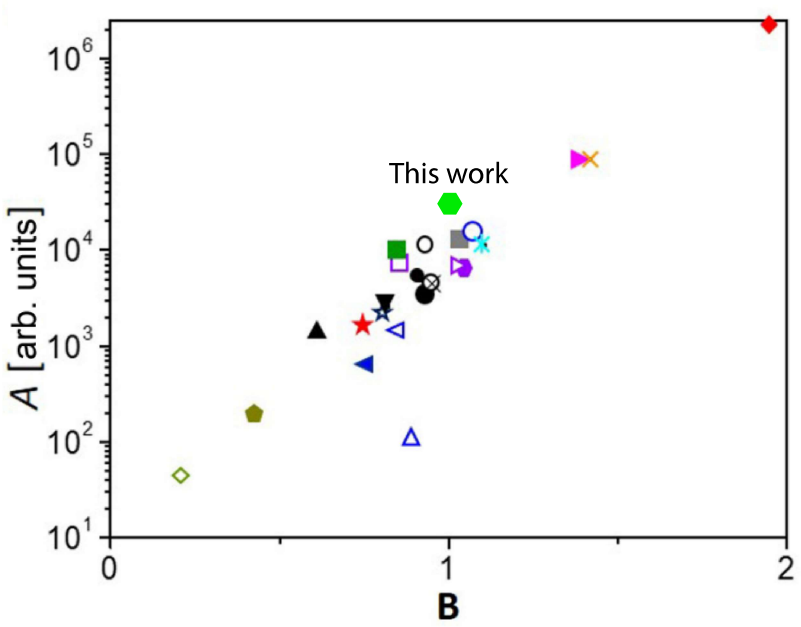


**Figure 2.13:** Comparison between the results obtained for our samples of sputtered NbTiN with the results obtained from Ivry et al. in their study

is expected for a material to be almost constant and close to A parameter, according to Equation 2.7, while in our set of data a large dependence on $N_2$ flow was observed showing a dome-shaped curved, then either a dependence of A or B (or both A and B) is expected to be present. This needs to be performed to verify that the off points in the graph are due to not stochastic variation of thin film properties.

## 2.5 Optical Characterization

Due to the difficulty in being able to verify the results from ellipsometry, the analysis started with a literature review of results for optical characterization of NbTiN thin films. In particular, one of the most complete work was published by Archan Banerjee et al., [40], where they analyzed the complex refractive index of, among other materials, NbTiN using variable angle spectroscopy ellipsometry (VASE). The results they obtained showed a general increase of both $n$ and $k$ with the impinging wavelength. In this study they used a constant current magnetron co-sputtering of Nb and Ti in $N_2$ and Ar atmosphere, for this reason some differences are expected to be present, since the sputtering technique is different and also thickness of the

films may be relevant for this study, indeed this was used as a reference.

In our study the dependence of the room-temperature optical constants with the nitrogen content is shown in Figure 2.14. Some trends are possible to be observed, in particular, for what concerns the refractive index, it is possible to observe a local maximum in a range close to 300 nm wavelength, which is a near ultraviolet (NUV) frequency range, the value of the peak is generally independent from the nitrogen content. On the whole, up to $\sim$ 800 nm the refractive index of poor-nitrogen films is lower than nitrogen-rich thin films, thus showing a lower reflection of visible light. After $\sim$ 800 nm, then in near infrared (NIR) region, this trend is inverted and generally, nitrogen-rich films experience a lower $n$, contributing to a lower reflection of NIR electromagnetic radiation. Instead, all the films show a point of maximum of $k$, in the region between 375 and 400 nm (NUV region), the height of the peak is globally equal for all the $N_2$ contents and then, the higher the nitrogen content the higher the $k$, both in visible and NUV regime, thus nitrogen-poor films have a lower absorption of visible and NIR radiation. This is the proof that addition of $N_2$ in the film can significantly modify the atomic structure, influencing the optical properties.
All these results are valid for room-temperature NbTiN and not verified at cryogenic temperature, thus it is not possible to ensure *a priori* that the absorption (or the reflection) is enhanced (or minimized) also in cryogenic setup for single photon detection applications, and further study should be performed to check if the optical parameters play a dominant role in the metrics of final devices. Furthermore, reflection and absorption studies are valid only for simple designs of a SNSPD patterned on a specific substrate, but today high-SDE devices are characterized by embedding the SNSPD in an optical cavity (realized by stack of dielectric layers with different thicknesses, mainly Si, $SiO_2$, $Ta_2O_5$) with a reflecting mirror (that for 1550 nm is commonly made of a gold mirror) to maximize the absorption on the device layer and then the maximum count rate (or, alternatively, the detection efficiency).

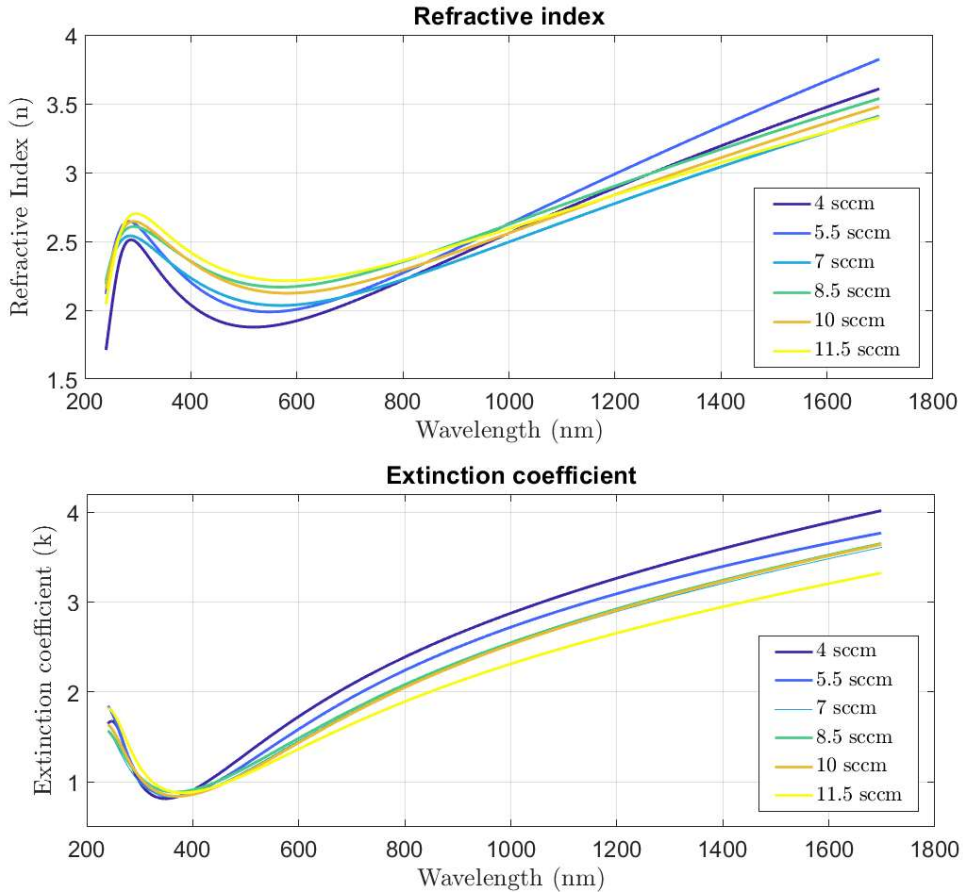


**Figure 2.14: Top**: Refractive index ($n$). **Bottom**: Extinction coefficient (k). The dependence of the optical constants with the impinging wavelength is evaluated using VASE technique

# Chapter 3

# Fabrication technology of superconducting microwire single photon detectors

The fabrication of single photon detector is a one-layer process, i.e. it is made of a thin film deposition, lithographic patterning and etching for transferring the resist pattern on the superconducting thin film (in this case, sandwiched structures, design of optical cavities or suspended devices are not involved). On the other hand, the choice of chemicals and tools must preserve the superconducting properties of the films. An example is the $O_2$ asher, which uses $O_2$ plasma for the stripping of the resist and often used for resist stripping on semiconductors, but this technique is not compatible with superconducting thin film processing, since it was shown that, upon ashing directly the superconducting film the $T_c$ was significantly reduced and the $R_s$ was increased, affecting the yield of the final devices. The $O_2$ asher solution could be used, for example, in case of application of a Si capping layer on top of the superconducting layer, but this would make the fabrication process longer since the silicon behaves as an insulator, not allowing for proper ohmic contacts (this leads to an additional lithographic and etching step, making the fabrication process much more complex). For this reason, generally baths in heated N-Methyl-2-pyrrolidone (NMP) are preferred. In addition, to ensure optimal quality and long-term repeatability of sputtered film compounds, the introduction of polymers in the reaction chamber is not allowed, thus precluding the possibility of performing lift-off techniques for realization of superconducting devices. In the following chapters the steps required for fabrication of superconducting nanowires are explained in details.

## 3.1 Pre- and post-deposition cleaning

The starting point for the fabrication of SNSPDs is a $SiO_2$ on Si wafer, realized by thermal oxidation, which is priorly cleaned using RCA standard cleaning and piranha solution and it is necessary to remove all the contamination which may alter the quality of the superconducting films or diffuse in the sputtering chamber, thus contaminating the sputtering system. This harsh cleaning procedure is not compatible with superconducting thin film processing, then they can be run only before the deposition of superconducting films. After this first pre-deposition cleaning step the wafer is covered with photoresist and diced in 10x10 $mm^2$ chips, the use of photoresist is uniquely to avoid the presence of debris on the final layer. Before the sputtering of chips it is mandatory to remove the resist which is spun prior dicing of the $SiO_2$/Si wafer, for this task the following cleaning procedure is run:

- Sonicated bath in Acetone for 5 minutes;
- Sonicated bath in Isopropyl alcohol (IPA) for 5 minutes;
- Blow dry with $N_2$ gun.

After the cleaning of the starting wafer, the dicing in 1 $\times$ 1 $cm^2$ and the removal of the resist (i.e. pre-deposition cleaning), the chips can be put into the sputtering chamber and the sputtering of superconducting film may occur. Since the sputtering system is located outside of the cleanroom, it is inevitable the contact of the chips with the external environment, making cleaning procedure highly recommended before performing the following steps (i.e. post-deposition cleaning). The aforementioned cleaning procedure may be repeated every time it is necessary. The artistic schematic of the overall fabrication process is shown in Figure 3.1.

## 3.2 Optical Lithography

Since the first realization of a working SNSPD, several optimization techniques have been studied for patterning SNs, the dominant one is e-beam lithography (EBL), which is the only tool available that is capable of realizing features below 100 nm at non-foundry research level, thus without involving extremely expensive DUV or EUV lithography steppers, light sources and hard masks, which are required for commercial-scale lithography tools. In recent years, alternative techniques arose, such as $He^+$ ion patterning, which allows for direct writing on superconducting films

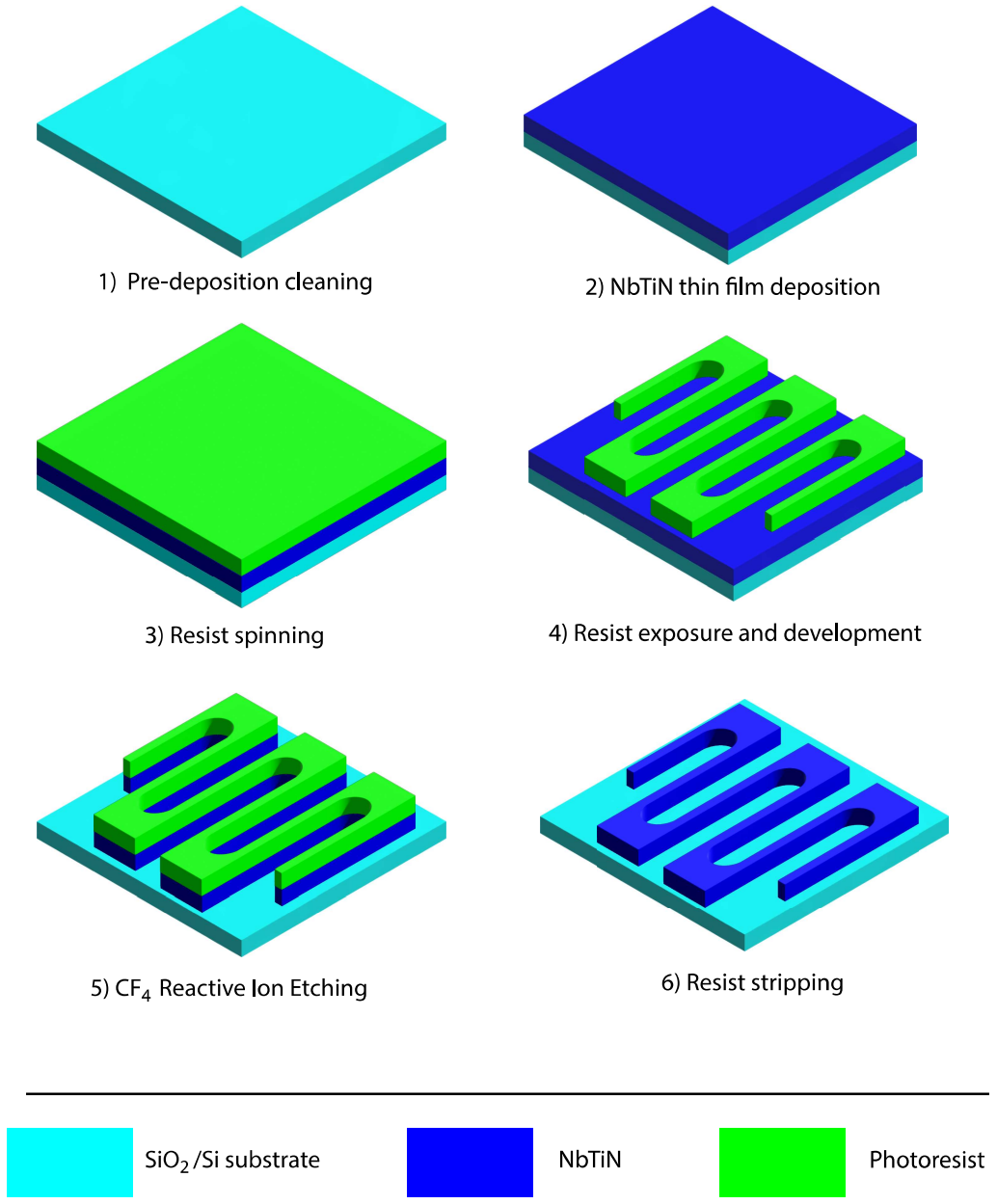


**Figure 3.1:** Artistic representation of the process flow required for fabrication of superconducting nanowire single photon detector

[41]. These two techniques suffer from the problem of slow patterning time, this is inevitable for high-precision at sub-100 nm level and EBL represents the best technology for small-area pixels with wire width below 100 nm. For designs which do not require such level of resolution, alternative techniques have been developed for years

and multiple works on optical lithography for patterning SMSPDs have been published. Most of them involve i-line steppers or laser lithography and they have shown the possibility to pattern photo-sensitive SMSPDs and microstrips [42, 43, 44]. The usage of optical lithography allows for overcoming problems related to fabrication of very-large-scale single-pixel SNSPDs, such as stitching problem: the writing area of a single field for Elionix HS50 and HS125 are 500 $\times$ 500 µm$^2$, this means that for writing a 1 $\times$ 1 mm$^2$ pixel 4 exposure fields are required, then lowering significantly the final yield, this problem is not present is maskless aligner tools or in traditional UV lithography tools. The tool used throughout this work is the Heidelberg MLA 150, which is an optical maskless aligner, thus not requiring the using of masks for patterning, whose realization is the most time-consuming and expensive part in optical lithography. In this case, thanks to an array of digital micromirrors it is possible to expose a binary pattern on a common UV-sensible photoresist using a 375 nm or a 405 nm laser, then commonly available photoresists can be used. This tool is generally faster than an EBL tool, and it allows for wafer-scale patterning in around 20-30 minutes, versus the hours which is generally demanded by our processes for SNSPD patterning at wafer scale. At the same time it does not suffer from stitching problem which can be detrimental for mm$^2$-area patterning using EBL tools. Our standard process is the following:

1. **Solvent cleaning** Solvent clean the substrate, check Chapter 3.1 for full description.

2. **Pre-spinning heating** Substrate heated at 110 °C for 60 seconds, this step is performed to to remove any adsorbed moisture or contaminants from the surface which may result in detrimental effects.

3. **Resist dispense and spinning** The photoresist AZ 3312 is dispensed on the substrate, covering 3/4 of the entire diameter. Then it is spun at 5000 rpm for 60 seconds using maximum acceleration. This high rotating speed is generally performed for ensuring a thin and uniform resist.

4. **Soft-Baking (SB)** Bake at 90 ° C for 60 seconds on a hot plate.

5. **Exposure** Expose with either 375 or 405 nm line, using a dose of 260 mJ/cm$^2$ for both the laser lines. Generally a dose test, ranging with a ± 50 % the nominal value, with proper step, on dummy chip is recommended before patterning good dies.

6. **Post-exposure baking (PEB)** Bake at 110 °C. This step is generally perfomed to make the resist more resistent to etching and avoid burning. Not required in case of lift-off.

7. **Develop** Photoresist is developed in AZ 726 MIF developer for 60 seconds at room temperature. Subsequently it is submerged in three baths of water to stop the developing.

8. **Dry** Dry the sample die with $N_2$ gun.

9. **Inspection** Optical microscopy inspection to check for under-development.

## 3.3 Reactive Ion Etching

After the patterning of the resists with different geometries the etching step is needed to be optimized to allow for optimal replication of openings in the resist. Independently from the used recipe, the first step is the cleaning of the chamber. In this stage an $NF_3$ plasma is striked in the main chamber and kept constant for 2 minutes, this step is performed for the removal of major contaminants, especially fluorine-based residues. Secondly, a conditioning step is run, performed with the same recipe of the etching process, for a time of about 5 minutes. After this conditioning step, the load lock can be vented and the samples are loaded in it, and the etching occurs. For this step two different technique were tried, the first one consists of one single etching step, whose length is set prior to loading the samples, this recipe is also referred as NBN_ETCH. The second solution consists of dividing the etching steps in multiple short (in the order of 20 seconds) runs, divided by a cooling step, both the cooling step duration and the plasma on-time can be tuned. Due to the presence of a cooldown step, this recipe is referred as NBN_COOL. The parameters were tailored to guarantee an etching rate of $\sim 2$ min/minute (the time considered is only the time in which the plasma is on, the cooling down time is only additional time). Thus, if the film has a thickness of 6 nm, a 3-minute-long etching process is required, this may divided in six 25-second-long etching steps, in between each etching step a cooling step is performed to cool down the sample. It is also a good practice to add some over-etching steps, to guarantee a full etching of the superconducting layer.

The main problem in the NBN_ETCH is that the high-energy $CF_4$ plasma reacts with the photoresist, which makes it very hard to be stripped upon etching, resulting in undesired layers of residual resist on top of the features. The NBN_COOL is

an optimized etching recipe which reduces the burning of the resist, thanks to the cooling between each cycle and the reduced on-time of the plasma, thus limiting the reaction of the resist only with the most superficial layer of the resist, this makes the stripping step much easier without affecting the final result. An additional solution to improve the heat dissipation is placing some drops of Santovac thermalization oil below the chip, the oil works as thermal contact with an underlying dedicated Si wafer and helps to dissipate faster the heat from the chip to the underlying wafer. The plasma bias power is set to minimum needed to correctly strike the plasma (25 W instead of 100 W), thus minimizing the reaction of the $CF_4$ plasma with the photoresist and the heating of the photoresist. All the other parameters are defined in the Table 3.1.

| **NBN_ETCH** | **NBN_COOL** |
|---|---|
| • Pressure: 2 Pa | • Pressure: 1 Pa |
| • $CF_4$ flow: 30 sccm | • $CF_4$ flow: 30 sccm |
| • Ar flow: 0 sccm | • Ar flow: 0 sccm |
| • ICP power: 0 W | • ICP power: 0 W |
| • Bias: 100 W | • Bias: 25 W |

**Table 3.1:** Comparison of etching parameters between the two etching recipes, highlighting the difference of bias power, thus resulting in a less energetic plasma.

## 3.4 Resist stripping

After either etching procedures of NbTiN layer the stripping of the resist was performed in a bath of N-Methyl-2-pyrrolidone (NMP) for 5 hours at 70 °C and left at room temperature overnight. At the end of the stripping procedure, to stop the stripping, acetone is sprayed on the sample die, to remove the NMP, and then sonicated in acetone for 5 minutes and in IPA for 5 minutes and dried with $N_2$ gun. After this step, the process is completed and the chips are inspected using scanning electron microscopes (SEMs). One of the main obstacles in this fabrication process is the resist burning, due to the reaction between the $CF_4$ plasma and the photoresist, which leads to detrimental effects in fabrication processes, as it is possible to

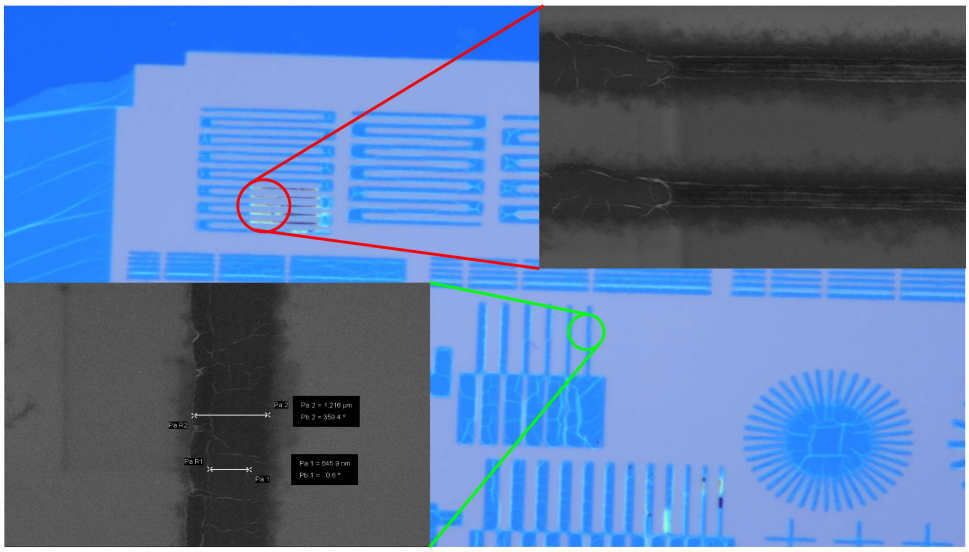

**Figure 3.2:** Optical and SEM images showing the presence of burnt resist and some lateral spreading of the resist during the stripping.

observe in Figure 3.2. The plasma used in the chamber, by reacting with the photoresist makes the stripping of the resist extremely hard with NMP, for this reason a lot of the effort was made in finding a solution to this problem, based on NMP baths.

## 3.5 Fabrication optimization

In the following chapter the techniques for the optimization in the etching step to avoid the burning of the resist are provided with major results for dose optimization using maskless optical lithography and the technique of overexposure to pattern features below resolution limit.

### 3.5.1 Etching recipe optimization

The first trial of etching was performed using a unique cycle with NBN_ETCH recipe in $CF_4$ plasma, time was taken according to an etch rate of $\sim$ 4 nm/min measured for NbN. Clear evidences of burnt resist occurred, then this recipe was abandoned in favor of slower but less aggressive etching NBN_COOL, which has reported better results for NbN and MoSi etching. Multiple combinations of plasma

on-time, cooldown time and Santovac usage were tried, the full list of trials is explained below.

1. **Usual NBN_COOL recipe** During this step, the recipe commonly used for etching of NbN using e-beam resist was performed, in particular 25 second of $CF_4$ active plasma and 120 seconds of cooldown step. The resulting film showed clear evidence of burnt resist.

2. **Long cooldown and no PEB** Cooldown and post-exposure bake were believed to be the major responsible for resist burning, then removed from the lithographic process flow and the cooldown step was lengthened to 300 seconds instead of 120 seconds. Strong evidences of burnt resist were on chip.

3. **Long cooldown, no PEB and Santovac oil** Cooldown was left at 300 seconds and PEB removed, but now the Santovac thermalization oil was added. This resulted in an improvement of the removal of the resist and few areas of the chip were free of the resist, but yet not sufficient.

4. **Long cooldown, no PEB and Santovac oil re-change** All the parameters were left unchanged with respect to the previous process, but now the Santovac oil was changed each two operation cycles. This was performed to have always the best thermalization with the underlying wafer. Not significant changes were visible with respect to process without Santovac change.

5. **Long cooldown, PEB present, Santovac oil and short plasma on-time** For this recipe the PEB step was performed, in order to strengthen the resist, the Santovac was not changed during the process and the plasma on-time was reduced to 18 seconds, instead of 25. For the first time, the totality of the burnt resist was removed. To verify the correct operation of this process, this same identical recipe was performed with 18 seconds and 20 seconds on-time plasma and in both cases only few traces of resist were left on the sample die.

### 3.5.2 Micron-scale-patterning

Before starting with trial-and-error optimization of the exposure parameters, as preliminary step the datasheet provided by the manufacturer was read. In particular

AZ Electronic Material, manufacturer of the used photoresist, provides a suggested process using i-, h- and g-line wavelengths, which means 365 nm, 405 nm and 435 nm wavelengths respectively. The tool is provided both with 375 nm and 405 nm laser, which means that g-line data are automatically excluded from the choice. As positive tone resist we used AZ 3312. The recommended recipe for a i-line exposure, which corresponds to a wavelength of about 365 nm, which is approximately the same laser line present in the MLA (375 nm) and consists of four consecutive steps: a soft bake (SB) at 90 °C for 60 seconds, exposed with desired dose, post-exposure bake (PEB) at 110 °C for 90 seconds and development using the AZ 300 MIF or AZ 726 MIF for 60 seconds at room temperature.

The first step in the optimization for lithographic patterning was the realization of layout which could be useful as a starting point. The layout was realized through PHIDL package in Python with a total footprint of 200 × 400 µm$^2$. The layout is mainly composed of stars, straight vertical and horizontal lines, meandered microwires, squares and circles which can be compared to analyze, as a function of lithographic parameters, the minimum size that can be safely patterned on NbTiN films after $CF_4$ RIE. After the definition of a suitable layout, a dose and defocus test was performed. The defocus is the variation of the height of the stage with respect to the focal plain of the optics system, a positive value means that stage is higher than optimum focal plane (then, closer to the optics), negative values that the stage is below the optimum focal plane (then, further from the optics), zero means at focal plane.
The first trial was performed on a wide spectrum of doses, in particular from 125 to 350 mJ/cm$^2$, with a 25 mJ/cm$^2$ dose step, defocus was kept between -3 and +3 (a +/- unity is a fixed height difference from focal plane), with unity increment. Before etching, the patterned features were then inspected through SEM. After a first inspection, the doses which did not causes evident under-exposure or over-exposures were measured more in details. Examples of under- and over-exposures are shown in Figure 3.3, where for very low doses features are not open and indeed upon etching it acted as mask without allowing for etching of underlying film. For severe over-exposure the feature are clearly smaller or not present on the resist. For 375 nm linewidth, the best doses recorded are 250, 275 and 300 mJ/cm$^2$ with 0 defocus, whose some features' size is analyzed in Table 3.2 and some images of the results (resist still present on top) are shown in Figures 3.4, 3.5, 3.6.

After this preliminar step, a new dose test was run, this time using as a layout

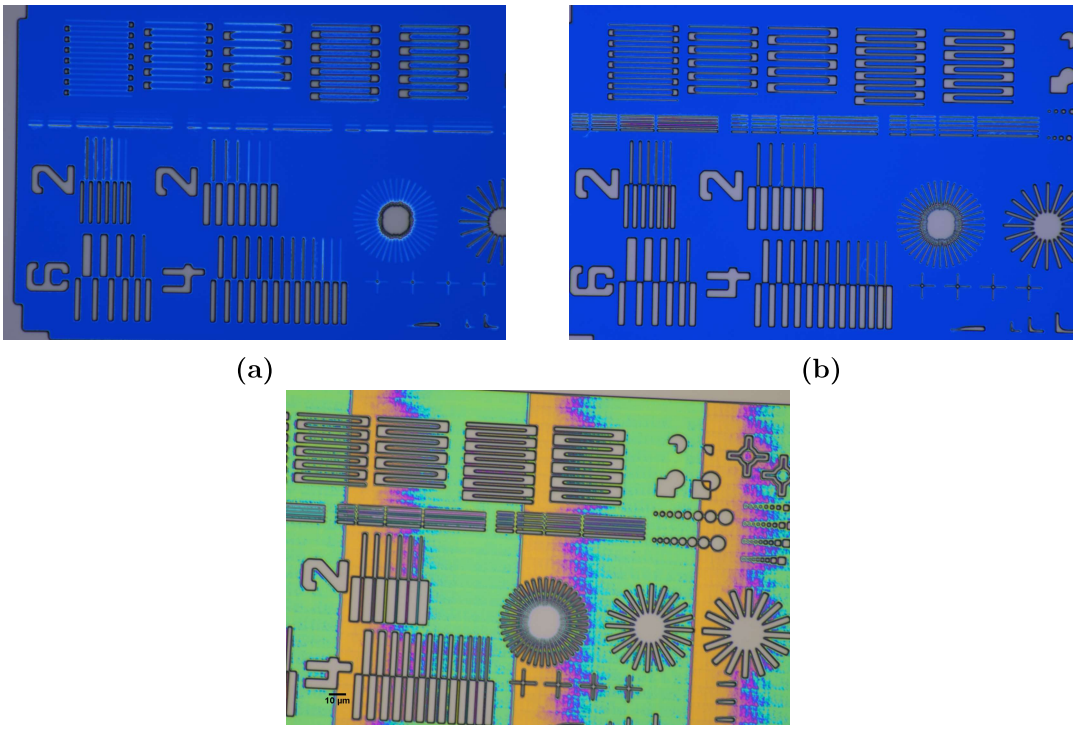


**Figure 3.3:** Optical micrograph of dose test patterns after development. In blue NbTiN layer, in white AZ3312 photoresist. (a) Dose: 350 mJ/cm$^2$ Defocus: 0. Example of over-exposure: it can be noticed by the absence of the horizontal lines, which are present in (b) which shows an example of good exposure, with a dose of 275 mJ/cm$^2$ and defocus 0. (c) shows the test structure exposed with a dose of 125 mJ/cm$^2$, in which it is clear the diffraction pattern made by the undeveloped photoresist. All three images are taken with the same filter of optical microscope to highlight the presence of refractive patterns in undeveloped resists

| Dose | 0.9 µm width | 1 µm width | 4 µm spacing | 1 µm width | 2 µm spacing |
|---|---|---|---|---|---|
| 250 | 1.075 | 1.138 | 3.853 | 1.07 | 1.93 |
| 275 | 0.807 | 0.888 | 4.127 | 0.83 | 2.17 |
| 300 | 0.668 | 0.859 | 4.332 | 0.709 | 2.381 |

**Table 3.2:** Table of linewidths and spacings measured with SEM appartaus, the headings represent the size in the digital layout. Used for dose comparison using 375 nm wavelength laser of Heidelberg MLA150

a set of SNSPDs and microwire. In this case, the structures are SNSPDs, whose linewidth varies from 0.8 up to 3 µm and nanowires whose width varies from 0.7 up

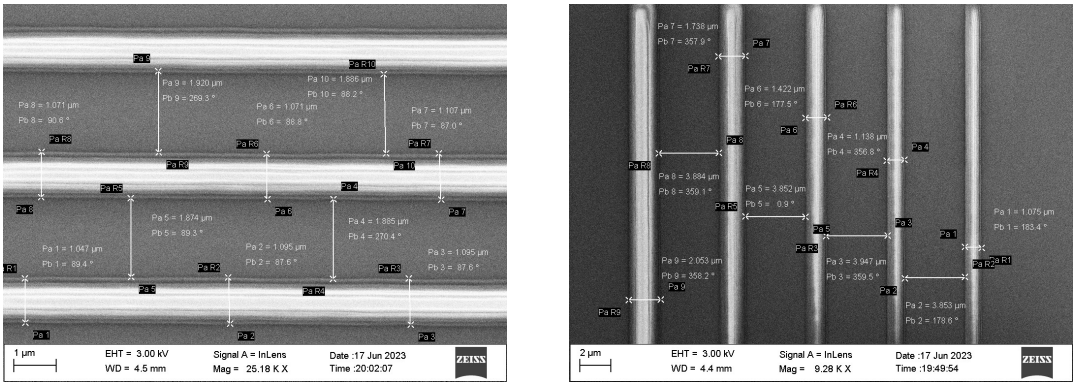


**(a)** **(b)**

**Figure 3.4:** Vertical and horizontal lines patterned using a dose of 250 mJ/cm$^2$

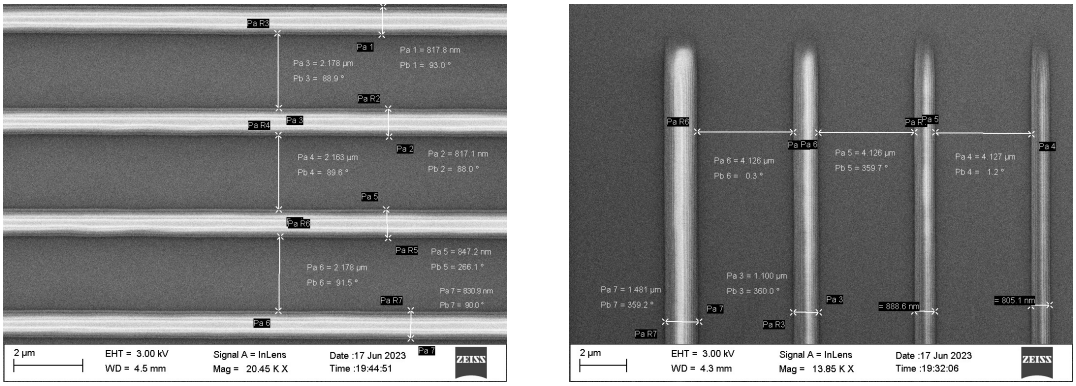


**(a)** **(b)**

**Figure 3.5:** Vertical and horizontal lines patterned using a dose of 275 mJ/cm$^2$

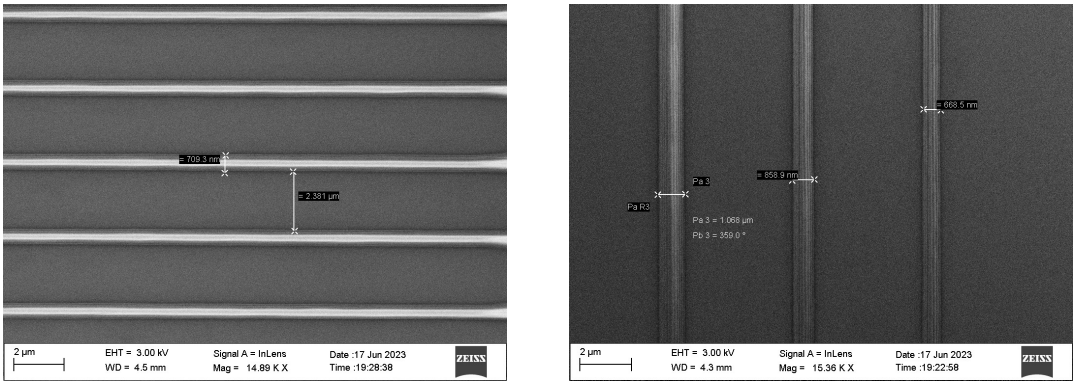


**(a)** **(b)**

**Figure 3.6:** Vertical and horizontal lines patterned using a dose of 300 mJ/cm$^2$

to 5 µm. In previous paragraphs it was shown that a good value for dose is around

250 mJ/cm$^2$, then a denser dose sweep was performed with ± 25 % was tried, i.e. from 200 up to 320, divided in 15 steps, which means one each 8 mJ/cm$^2$. This experiment is performed on both 375 nm linewidth and 405 nm linewidth, in order to check possible dose variation depending on the used laser line, showing that the best doses for the two lines are: 260 mJ/cm$^2$ for 375 nm and 260 mJ/cm$^2$ for 405 nm. With these doses it is possible to safely pattern features around 900 nm and slightly smaller. It is important to highlight that the resolution limit of the tool is 1 µm.

### 3.5.3 Sub-resolution limit pattering

After the dose test experiments on 375 nm and 405 nm wavelength, it is possible to notice that generally the best dose is 260 mJ/cm$^2$, and 260 mJ/cm$^2$ for 405 nm laser wavelength, but for specific designs it is always recommended to run a dose test around these two central values, in order to tune the proper process parameters according to the interested geometry. From the results obtained in Chapter 3.5.2 Table 3.2, it is possible to observe, that if the dose is not much higher than the optimum, the effect of over-exposure can be used to print features that are smaller than the layout size, but keeping the pitch constant, in the case of fabrication of SNSPD, thus reducing the fill factor. In case of patterning a single wire it simply appear smaller than the expected size in the layout. It was believed that this solution can be implemented to pattern features that are far below 1 µm without requiring high-resolution tools. It is important to add that over-exposure is a purely random process and strongly dependent on local thickness of the resist, then it is very hard to predict in exact way the final feature's size known the layout. As a proof of this concept, using a 405 nm linewidth some large-area SNSPD, with features smaller than 1 µm and a filling factor of 0.33, and sub-micron-width nanowires were patterned using a dose of 275 mJ cm$^{-2}$, which is generally beyond the optimum for this line. After etching step, the width of the wires were measured in multiple locations of the same device, in order to provide a dispersion in linewidth. The results are shown in Figure 3.7, 3.8 and 3.9. Before describing the results it is important to notice that the use of over-exposure is the only way to reach resolution in the order of 0.5 µm and that the wires with 1.25 and 1.5 µm width were close to the edges of the film, thus the result can be affected by irregularity of the film, mainly thickness in-homogeneity.

It is possible to notice instantly that also for large features the patterned wires are

smaller than layout size, even if the layout size is much larger than resolution limit of the tool, this highlights the fact that the ability to produce sub-micron patterns relies on the ability to over-expose the resist. Secondly, it is possible to notice that using over-exposure the actual resolution limit starts to get closer to the resolution limit of the resist, which is around 500 nm and not of the tool anymore, which is around 1 µm. In some cases the patterned features were even smaller than the resolution limit of the resist, but with a large variance in the feature's size. Some groups have declared to reach a 0.4 µm linewidth/spacing using a 0.5 µm-thick resist, which is twice thinner than the one used in this work, then possible improvement in this alternative patterning technique could be focused on using thinner resists in order to further optimize this process. This result is the proof of the possibility for further optimization of this process for safely patterning features as small as 500 nm, but the process requires to use very thin positive resist (commercially available UV sensible resists are AZ 1505, which can guarantees positive-tone resists as thin as 400 nm or AZ ECI 3007 and AZ 701 MiR, which upon sufficient dilution can guarantee final resist thickness around 200-300 nm).

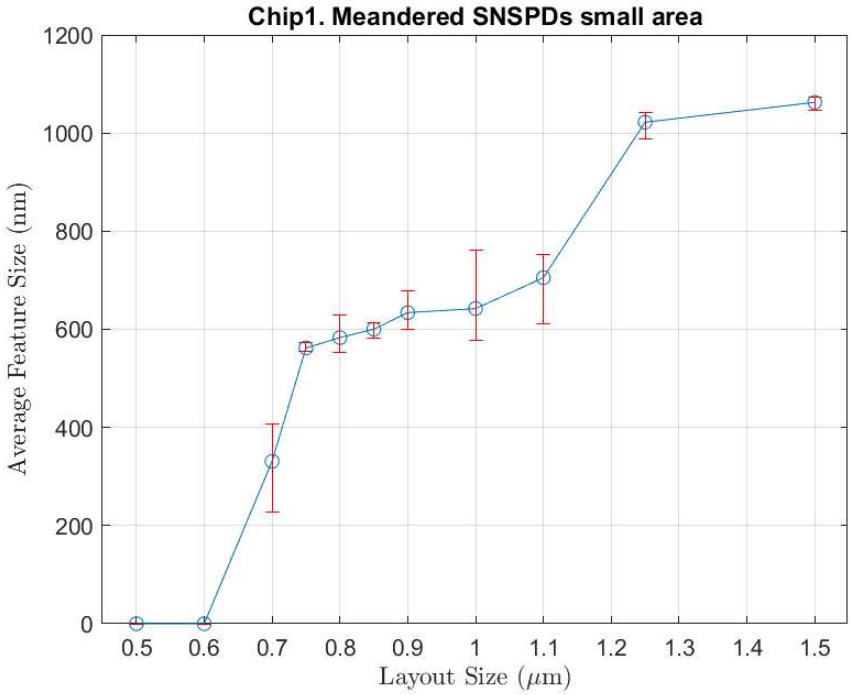


(a)

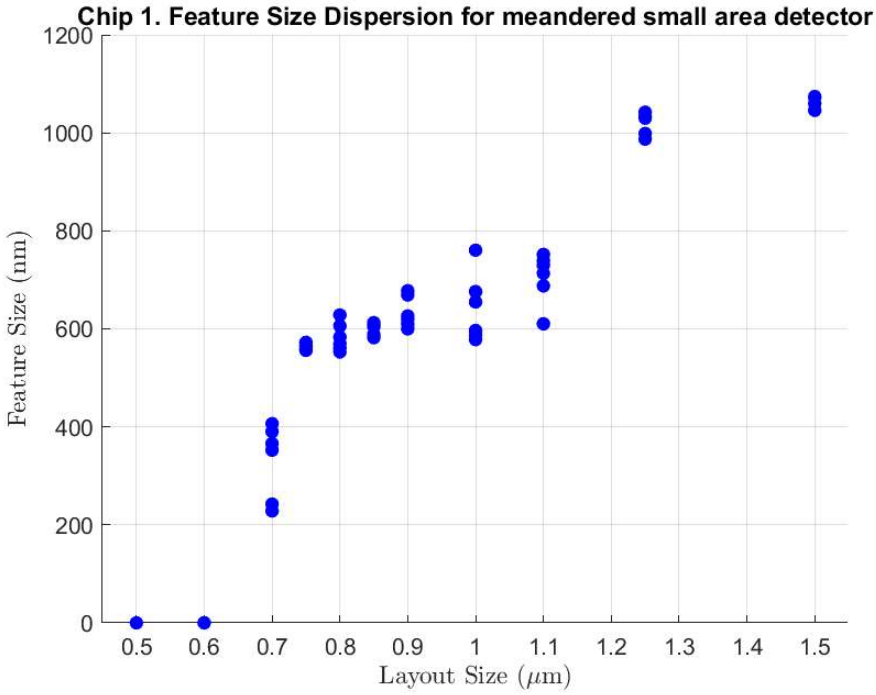


(b)

**Figure 3.7:** Average size of developed features on small area detector (a) and large area detector(b). The red error bar does not represent the standard deviation since the number of point is not high, but it represents the minimum and the maximum of the measured width

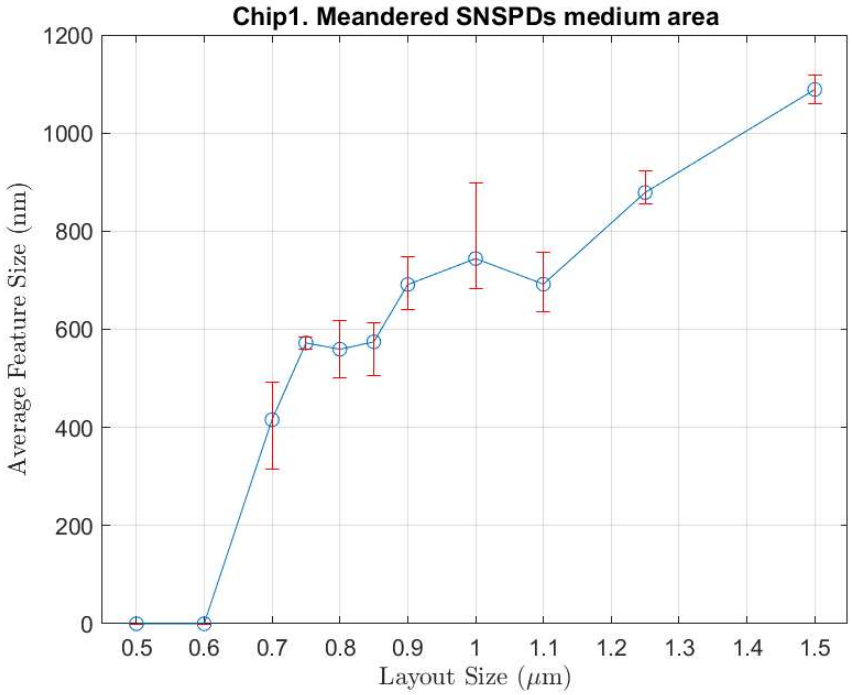


(a)

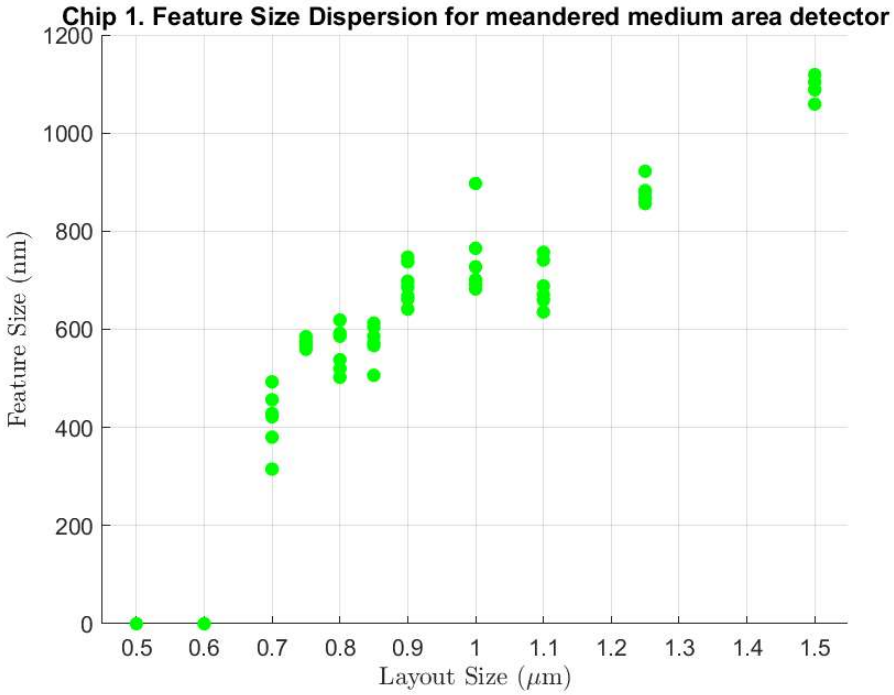


(b)

**Figure 3.8:** Distribution of measured width for the small area detector (a) and large area detector (b). Each point represents one measurement for a defined layout size

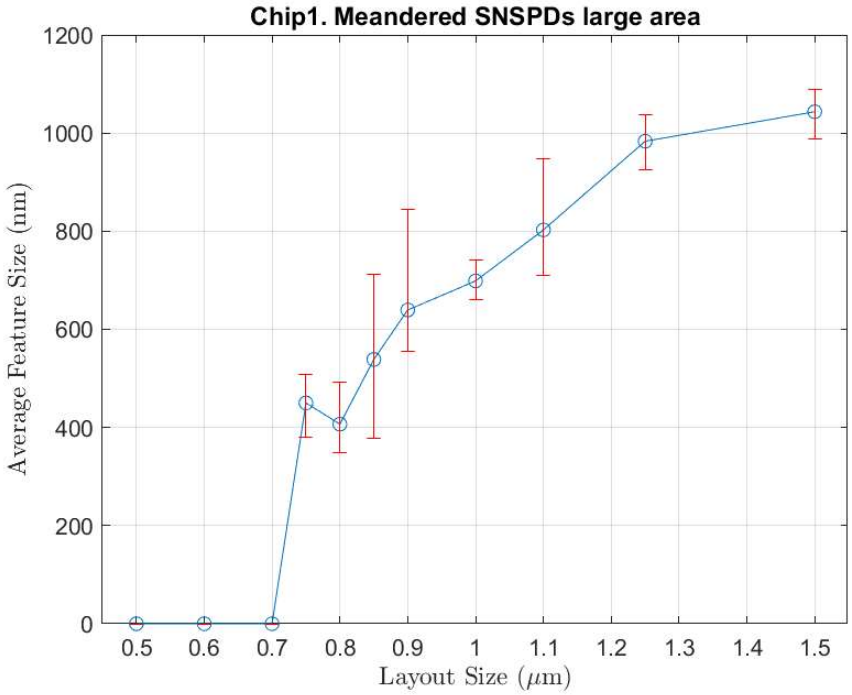


(a)

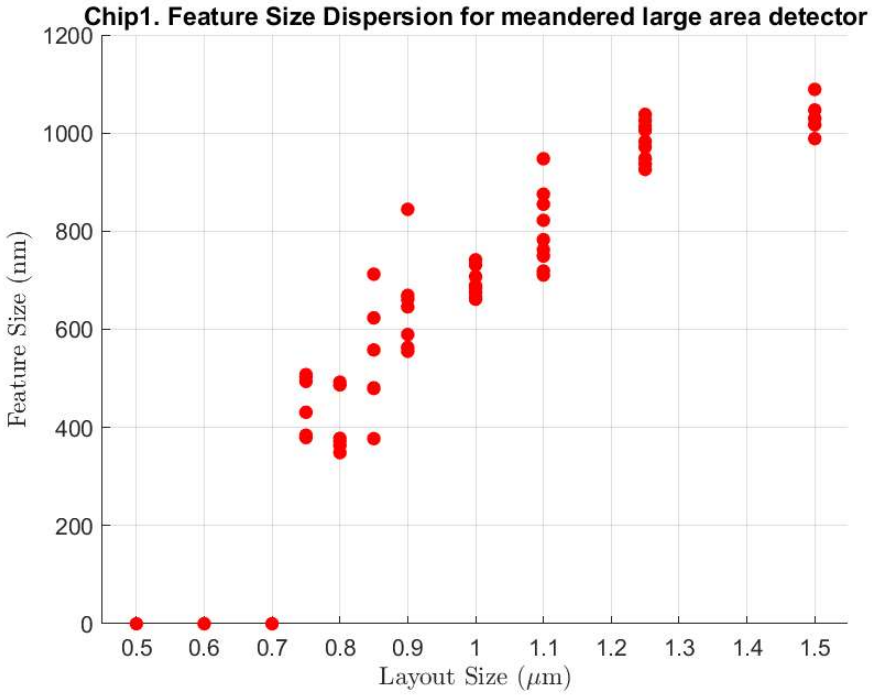


(b)

**Figure 3.9:** Distribution of measured width for the small area detector (a) and large area detector (b). Each point represents one measurement for a defined layout size

# Chapter 4

# Photon-detection and electrical characterization of superconducting microwire

## 4.1 Design and fabrication

Using the optimized recipes for patterning using optical lithography tool, different configurations of straight and meandered wires were designed using Python packages PHIDL and QNNPY. One important parameter in the design of SNSPD is the reset time, $\tau_r$, which is defined as $\tau_r = L_k/R_L$, where $L_k$ is the kinetic inductance of the nanowire, while $R_L$ is the load resistance of the wire. If the reset time is too fast the device will be unable to self reset. For this reason, to avoid latching two viable solution are generally used, increasing the inductance or reducing the load resistance. The inductance can be increased by an inductor in series to the wire, this is done by patterning a meandered wire, whose width is sufficiently larger than the width of the nanowire (generally, three times larger is sufficient) in order to inhibit the generation of pulses, which may influence the photon count rate (PCR). The inductance can be tuned by evaluating the sheet kinetic inductance of the film from the formula $\mathcal{L}_k \approx 1.378\ R_s/T_c$ (the result is in pH/square). Once $\mathcal{L}_k$ is known, it is possible to design at the same time both the total area of the inductor (i.e. the total number of squares) and the load resistance of the wire, generally by using a shunt resistor, which can be soldered in the PCB between the pad and the ground pads in the PCB, or alternatively using in-line shunt resistors. General values for $\tau_r$ that do not lead to latching are between 10 and 100 ns. The choice of the shunt-resistance, $R_{sh}$ and the series inductance $L_k$ not only allows for tuning the $\tau_r$, but also the

final device performances can be affected. Indeed, a large series inductance may be responsible for the reduction of the slew rate on rising edge of the pulse, and at the same time increasing the reset time, thus limiting the count rate. In the same way, the choice of the shunt-resistor is subject to a trade-off: a small shunt-resistor prevents from latching and increases the current range, however it can degrade the performances by lowering the count rate and increasing the jitter, since the lower the shunt resistance the lower the pulse and higher the reset time. Wang et al. [45] studied the effects of the shunt resistors and series inductance on bare microbridges, demonstrating that:

- In absence of a series inductance (resistance range between 20 and 2 Ω), the reduction of the shunt resistor leads to a decrease of the DCR or, alternatively, an increase in the the bias current range. Same results were obtained with the presence of a fixed series inductance. On the other hand, a smaller shunt resistor reduces the pulse height and increase the exponential decay time, degrading jitter and count rate of the device.
- Two identical bridges (same width and critical current) were tested with and without a series on-chip inductor. The presence of a series inductor improved the stability by preventing latching mechanism, from the values provided the reset time is about 50 ns.

On the other hand, as highlighted by the authors themselves, in the studied no optimal combination of $R_{sh}$ and $L_k$ was estimated or a theoretical model was extracted.

## 4.2 Experimental setup

### 4.2.1 Cryogenic setup

Once the chip has been fabricated, and checked for absence of detrimental fabrication errors, it needs to be mounted on a cold head of a cryostat. The cold head is the central cooling component of a cryostat and designed for the maximum cooling power and lowest temperature to a single mechanical stage. The cryostats used in this work are a single shot He-3 cryostat, with a base temperature of 300 mK and 3 K, manufactured by Janis, and a cryostat manufactured by ICE Oxford, which has a large 1.3 K stage. For correct measurements a proper thermalization must be ensured and as many as possible electrical connections must be provided. For this task, ad-hoc PCBs have been designed during the years for guaranteeing a

proper number of electrical connections and good fit with the stage of the cryostat. The sample die is mounted to the PCB with GE varnish on a region plated with electroless nickel immersion gold, subsequently each of the contact pad realized on the chip are connected to pads in the PCB through wire bonding. The unpatterned region is wire-bonded to the ground connection through multiple wire to allow a more stable value of the ground on the entire chip. Each PCB for the cryostat is featured with push-on RF connectors, which allow for pulses readout. Once the PCB is mounted to the cold head of the cryostat, the die samples are illuminated via free-space coupling from a fiber mount designed to fit the PCB footprint, using a visible eye-safe laser. This step is required for aligning the light beam with the sample die before sealing the cryostat. Before sealing and cooling the cryostat, the electrical resistances are measured to check for electrical disconnections or grounding of a device. At this stage, the cryostat is sealed and cooled down for at least 24 hours until the base temperature is reached.
Beside the two cryostats for higher temperature measurements, a dip-stick probe was used. The principle for thermalization is exactly identical, the only difference is that it is a probe that can be submerged into a liquid helium dewar, thus used for measurements at temperature of 4.2 K or higher. The main advantage of this setup is that it does not require the long time vacuum and cooling time of the cryostat and the probe is equipped with 28 RF output lines, which are used to monitor electrical signals from the devices (for the ICE Oxford and Janis stage "only", respectively, 8 and 6 RF connectors are available), a diode thermometer is mounted for a correct temperature measurement, an optical fiber runs along the probe for optical measurements and a magnet is mounted for measurements that require the presence of a magnetic field. This probe allow for faster measurement since it is necessary only the time for pumping it down, which is generally couple of hours and then it can be submerged in liquid helium for measurements. In both the case of the cryostats and the dip-stick probe all the measurements are run through dedicated Python codes, which controls the measurement equipment.

### 4.2.2 SNSPD measurement setup and process flow

For optical characterization, a sub-picosecond fiber-coupled mode-locked laser was used with wavelength of 1550 nm (ThorLab S1FC1550) and 780 nm (ThorLab S1FC780). The single-mode optical fiber, which is coupled to the laser, runs along the cryostat and the fiber is manually aligned before sealing the cryostat, this step is performed by coupling a low-power eye-safe visible laser to the input of the fiber

and observing if the chip is entirely impinged by the laser spot. Once the beam is aligned to the chip, the cryostat is closed and the room temperature resistances are measured, in order to ensure that there are not errors in the electrical connections before cooling down the cryostat. Each of the device were biased using a low noise voltage source (Yokogawa GS200) and a room-temperature bias resistor, generally in the order of 10 - 100 kΩ, while the RF output signals were carried out by stainless-rigid coaxial cables. The DC and RF signals were decoupled using a bias tee (ZFBT-6GW139 from Mini-Circuits). The output RF signal is then amplified by a low-noise amplifier (LNA), LNA-2500, before being connected to the oscilloscope (LeCroy WaveRunner 620 Zi) or a counter (Agilent 53230A). The choice of the amplifier is a vital part of the setup, since it is generally the component that introduces the largest amount of noise on the RF signal and it is necessary that it is low-noise within a large bandwidth (typically from DC up to some GHz). In some setups, it is also possible to integrate cryogenic amplifiers in the cryostat for further reducing the electrical noise (noise $\propto$ kT), generally made of a two-stage amplification with DC-coupled HEMT and SiGe LNA. In our setup, an in-line shunt made of a 50 Ω and 1.2 µH was present. An artistic schematic of the full setup is shown in Figure 4.1.

After measuring the critical currents and checking that the normal state resistance is coherent with the one measured before cooling down, it was time for checking the photon-counting ability of the devices. Using an oscilloscope the trigger was set to a level that allow not to collect noise floor from the electronic setup while visible dark counts are measured. The bias current is kept in a level that allows for measuring some dark counts, generally $\approx 0.9\ I_c$. The output is monitored using a 50 Ω coupled oscilloscope. The shape of the pulses tells us if the device is self-resetting, if it is not, the device is not able to sustain dark counts and will latch after some counts. The height of the pulse is equal to the product between the bias current and the hotspot resistance, $I_b\ R_{hs}$, with $R_{hs} \simeq 10$ kΩ, generally the higher the pulse the easier the distinction with the noise floor. The shape of some pulses is then stored, in a way that reset time can be measured. From the shape of the pulses it is also possible to resolve photon number [46]. If it is possible to distinguish a pulse from the noise floor, it is rapidly checked if the device is able to count photon, by turning on the laser and biasing the device close to its critical current. If when the laser is on, more pulses appear in the oscilloscope, the device is sensitive to photons and the RF output signal can now be connected to the counter. Between the RF output of the SNSPD and the input of the counter a large-bandwidth low-pass filter (bandwidth

from DC to a frequency much larger than maximum count rate) is connected for filtering out the noise on the pulse. The usage of a low-pass filter is recommended because the counters injects some noise in our measurement and it is desired to filter it out.

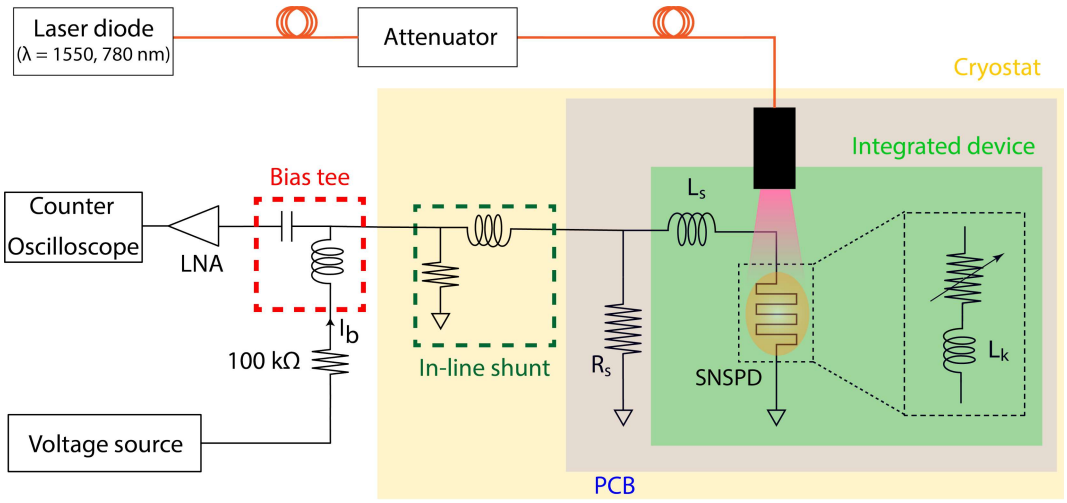


**Figure 4.1:** Schematic representation of the setup used for SNSPD characterization. $L_s$ and $R_s$ are the series inductor and the integrated shunt resistor, if present. In blue it is highlighted the the chip which is on the PCB and it is in the cryo stage. The in-line shunt is made of only a 50 Ω resistance and a 1.2 µH inductance. Then the bias tee, which for our setup is a ZFBT-6GW from Mini-Circuits. The bias resistor is 100 kΩ and used to bias the setup with the correct current.

Once organized the setup, it is important to set the voltage threshold for the counter, any pulse that overcomes the threshold will be considered as a count, than in order to measure only the pulses originating from our SNSPD a threshold sweep is performed, starting from 0 V up to voltage values above the pulse. In this way, for very low values of the threshold, both the noise and the pulses will be considered, then the count rate will be very high. Increasing the voltage threshold the count rate will decrease following a gaussian dispersion. When the threshold level is correct no noise is collected by the counter but only the pulses, this region is characterized by a plateau of counts. If the threshold is then too high no pulse and noise will be registered, leading to a zero count rate. This process is run with the light on and light off (using the blocking function of the optical attenuator), in order to appreciate in both cases a variation of photon counts. The threshold of the measurement is then placed in correspondence of the plateau, generally keeping sufficient margin from the noise floor. At this stage, the PCR measurement is run through

a Pyhton code, which once set the threshold level, used by the counter, ramps up the bias current up to critical current and for each value of current it counts the pulse generated upon photon absorption. When using the 1550 nm wavelength, the code runs firstly the total count rate for a certain attenuation, then it blocks the light, using the optical attenuator, which fully blocks the radiation coming out from the input fiber. For shorter wavelength this process is run by the operator by manually turning on and off the laser. In this way it is possible to count the real pulses as the subtraction between the total counts and the dark counts. To ensure that the device is correctly working in single photon regime, the attenuation is ramped from 0 dB (same optical power from the laser diode) up to an attenuation value that allows for small number of counts (generally around 10 - 20 dB), for each value of attenuation the count rate is measured for a fixed current generally close to $I_c$. If the count rate is linear with attenuation and the count rate is halved each 3 dB of attenuation than it is sure that the device is working in single photon regime.

## 4.3 First results

The first measurements in dip prob was performed with a sample with one of the highest sheet resistance, 1.3 kΩ/sq despite a low $T_c$ of 5.5 K. Firstly, the chip was mounted on the dip-stick probe and submerged in liquid helium (T = 4.2 K). This first test did not lead to any significant result, indeed all the microwires seemed to behave as a resistor, whose resistance is close to 100 kΩ and not as a superconducting microwire, suggesting that operating temperature is too high for correct operations. Due to problem in measuring the performances of the device in the dip probe, a second attempt was were then run in ICE cryostat, which allowed to cool down the sample down to a base temperature of 1.3 K. I-V sweeps were run then at temperature of 1.3 K and results are shown in Figure 4.2.

The results show a very small critical current, from 0.7 µA up to 14 µA, while much higher currents were expected, suggesting that something went wrong during either sputtering of the film or fabrication or storage. Most reasonable solution is that these samples were deposited little time after the opening of the main chamber, which may have caused oxidation or degradation of the NbTi target, resulting in a very low quality film. The alternative hypothesis is that the fabrication or the storage of the film altered the properties, this suggests that in future it is always

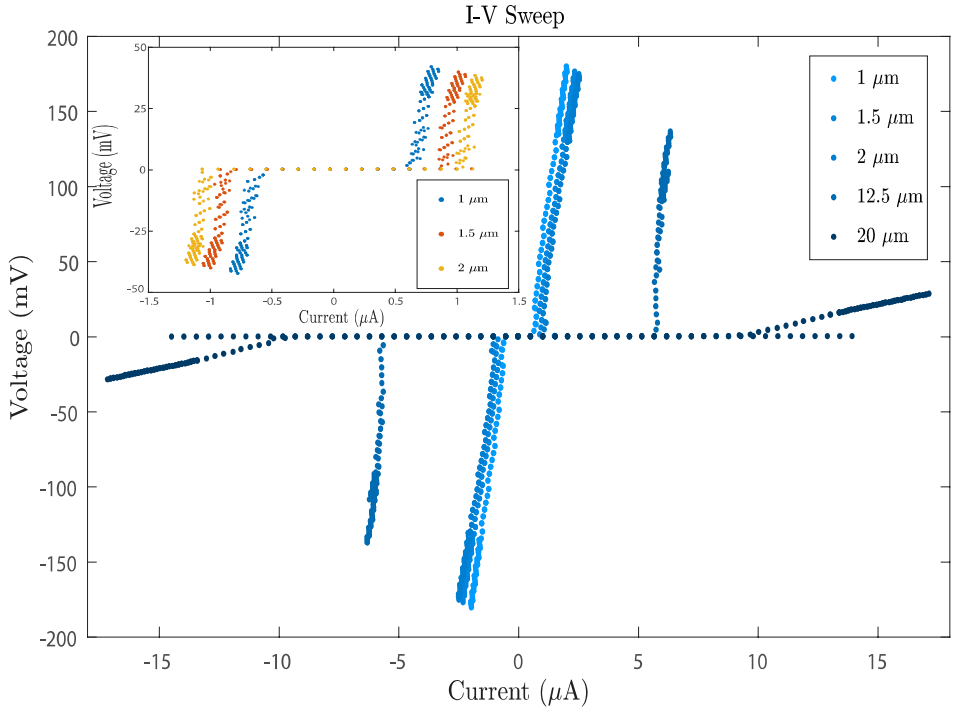


**Figure 4.2:** Full I-V sweep of microwire. **Inset** Zoomed portion of the I-V curve for wire widths of 1, 1.5 and 2 µm

better to complete the fabrication process (lithography and etching) and measurement as close as possible to the sputtering of the films, since the contact with air may deteriorate easily the film, for example by formation of the oxide on top of it. Upon I-V curves measurements, the chip was coupled with three different laser lines, 1550 nm, 780 nm and 406 nm, but in none of the cases photon sensitivity was observed. Secondly, since all the microwires had the same length, the overall resistance of the wire should depends on the number of squares that a wire is made of. For this reason, the resistance of 20 µm-wide is significantly smaller than 1, 1.5 or 2 µm-wide. This is not true for example for 12.5 µm-wide wire, which shows a resistance comparable to the much smaller wires, suggesting possible fabrication-related errors. Another interesting result is the absence of hysteretic curve for all the widths but 20-µm-wide wire. On the other hand, it is possible to notice that as expected the critical current is proportional to the size of the wire, this is correct with SN theory.

## 4.4 Micron-wide NbTiN SNSPD

After the first results, two films were prepared and patterned using the recipe described in Chapter 3.5.3 for the realization of different devices. From now on they will be referred as Film 1, which is 8-nm-thick film, $T_c$ of 9 K and $R_s$ of 513.2 Ω/square, and Film 2, which is a 5-nm-thick films, $T_c$ and $R_s$ were 701.8 Ω/square and 7 K, respectively.

### 4.4.1 Film 1

On Film 1 both SNSPDs and microbridges were patterned. In particular three microwires, in this case two 1-µm-wide wires, one of the is shunted with the 50 Ω - 1.2 µH in-line shunt, while the second one not, the third one is a 1.5-µm-wide wire. The two 1-µm microstrips were used to study the possible effects of shunt resistors on microwires, without using an on-chip series inductor. On the other hand, two SNSPDs with a linewidth of 1 µm and one with a linewidth of 550 nm were tested, using the Janis cryostat. First, critical current measurements were performed for checking that sputtering and fabrication did not lead to catastrophic failure of superconductivity of the wires. The results are shown in Table 4.2. It is possible to notice that the shunted microstrip has a larger $I_c$, this verifies the results obtained by Want et al.

| Width | Shunted | $I_c$ | $I_r$ | $I_r/I_c$ | $R_{ns}$ |
|---|---|---|---|---|---|
| 1 µm | No | 25.2 µA | 14.2 µA | 0.56 | 33 kΩ |
| 1 µm | Yes | 28.2 µA | 28.2 µA | 1 | 49.1 Ω |
| 1.5 µm | No | 50.5 µA | 23.7 µA | 0.47 | 21.1 kΩ |

**Table 4.1:** Table for critical current measurement for microwire at 3 K. $R_{ns}$ is the normal state resistance.

The straight microwires appeared to be extremely latching, so the PCR measurement is inhibited. Generally, the shunted device appeared to work better, indeed it was the best one within the microwires, but the reset time was still too low, suggesting that a series inductor is required for correct operations, thus reducing the reset time $\tau_r = (L_{inductor} + L_k)/R_L$. Within the three SNSPDs, the one with smaller linewidth appeared not to be working correctly, showing a switching current of about

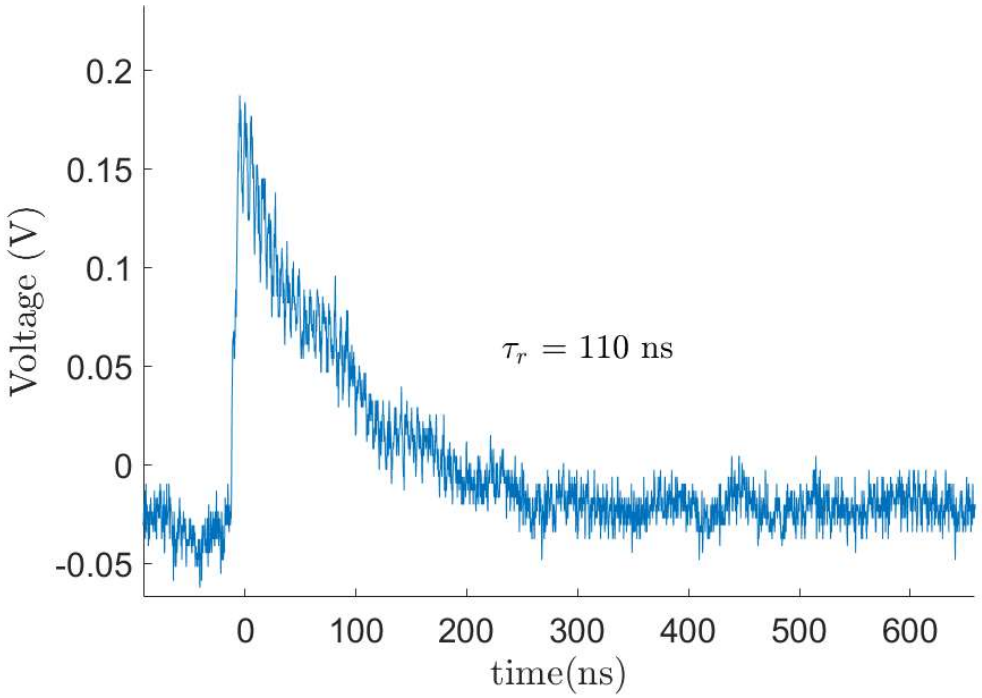


**Figure 4.3:** Pulse shape recorded from 1 µm linewidth SNSPD, detector area of 200 × 200 µm$^2$

2 µA, probably due to some fabrication defects. For the working SNSPDs, one was resulting in latching at high bias current, while the second one (which is larger) was optically characterized following the procedures explained in Chapter 4.2.2, using a LPF from DC to 48 MHz, given a reset time $\tau_r = 110$ ns, in this way part of the noise is filtered out but, the bandwidth is about 5 times the maximum count rate. Results of the photon count rate (PCR) were obtained using 1550 nm and 780 nm laser. The results showed an initial increase of the count rate with the bias current, but still far from saturation. For a clear visualization of the results, the bias current, $I_{bias}$ was limited to the values before device started latching. As expected, the sensitivity at 780 nm is higher than 1550 nm, but it is also possible to observe that the knee of the PCR curve at 3 K and in absence of shunt resistor is around 0.9 $I_c$, this phenomenon can be caused by multiple causes, mainly constriction within the device. Results are shown in Figure 4.4.

After this measurement the temperature was lowered to 300 mK, to study the temperature-dependence of the devices. All the microwires showed an increase of the critical current, up to double of the 3 K. On the other hand, the good-working SNSPD did not show any increase of the critical current and the count rate was in-

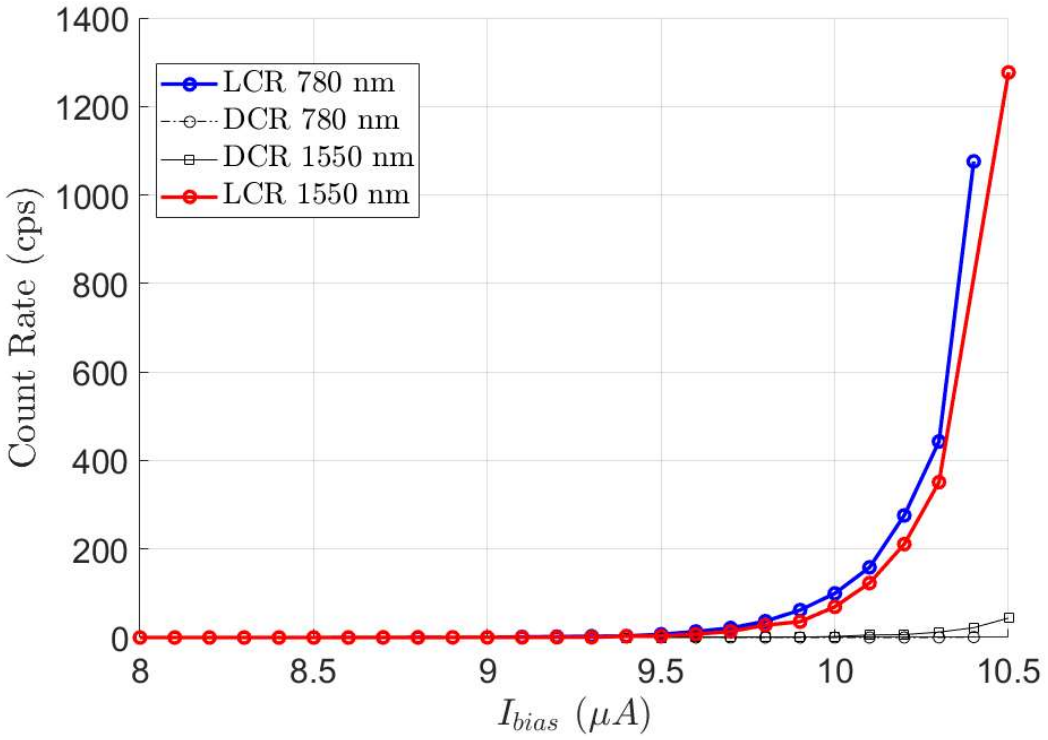


**Figure 4.4:** Photon count rate for a 1 µm wide SMSPD. The PCR is evaluated for both 1550 nm and 780 nm laser. The bias current, $I_{bias}$ is limited to the values thet did not make the devce latch.

hibited, this could suggest a misalignment during the transition to 300 mK with the optical fiber (when the cryostat was re-opened the fiber was loosened and this might have caused a loss of alignment between the device and the chip). The smaller device, on contrary showed a very large number of dark counts from oscilloscope monitoring and latching mechanism, which prevented it from being characterized.

| Width | Shunted | $I_c$ | $I_r$ | $I_r/I_c$ | $R_{ns}$ |
|---|---|---|---|---|---|
| 1 µm | No | 52.5 µA | 22.1 µA | 0.42 | 33 kΩ |
| 1 µm | Yes | 47.5 µA | 40 µA | 0.84 | 49.1 Ω |
| 1.5 µm | No | 87 µA | 24.7 µA | 0.28 | 21.1 kΩ |

**Table 4.2:** Table for critical current measurement for microwire at 300 mK. $R_{ns}$ is the normal state resistance.

### 4.4.2 Film 2

After showing that the straight wires were able to count photons, but due to the absence of any inductance, latching mechanism occurred for low current level, a new device was designed. Due to the low sensitivity of the films to the infrared radiation new films were sputtered using thinner films, in this case 5 nm, since it was shown that thinner NbTiN film show better sensitivity in mid-infrared regime [47] and with a sufficiently high critical temperature, in order to be able to be used in our cryostats. $R_s$ and $T_c$ were measured and equal to 701.8 Ω/square and 7 K, respectively, from here it is possible to estimate the kinetic inductance of the film, $L_k \approx 100$ pH/square. Two couples of straight microwire were patterned (i.e. two 1.5-µm-wide microstrips and two 2-µm-wide microstrips), all four detectors are connected in series with an on-chip 450 nH inductor. Each of the microstrips were shunted with 10 and 20 Ω. The inductor consists of a 500 × 500 µm$^2$ (approximately 4488 squares) meandered 5.5-µm-wide wire with a filling factor of 50 %, a picture of the final device is shown in Figure 4.5. Then, two couples of identical devices were shunted with different shunt resistances (10 and 20 Ω), leading to reset times of 22.5 ns and 45.0 ns.

Beside the four microstrips two meandered SNSPDs were patterned with a wire width of 1.8 µm and 2.2 µm, over an area of 650 × 650 µm$^2$ and 800 × 800 µm$^2$ with a filling factor of around 40 % to avoid large current crowding effects. The two SNSPDs are also much larger in area than the device patterned on previous film. This design choice was taken to counter the latching phenomenon of the previous devices by increasing the inductance of the wires. The first one was shunted with a 20 Ω resistance, while the latter on was shunted with the in-line 50 Ω - 1.2 µH shunt.

Unfortunately, also for this device once cooled down to the base temperature of 3 K all the devices worked as a resistor, whose value is the equal to the shunt resistor, despite $T_c$ was measured and equal to 7 K. In addition, in order to ensure problems in sensitivity of the multimeter, a second multimeter was used. In order to remove any measurement-dependent issues, it was tried to check for photon sensitivity of each of the device using the oscilloscope but no pulse was observed for any of the device, confirming in this way that all the patterned devices were resistors. As for the case of the first tested device, the films were patterned after the re-closing of the chamber. Then, it is believed that either a 5 nm thickness is too small and the deposition techniques need to be improved (for example using heated substrates) for ensuring correct operation, due to excessive lattice mismatch or other defects

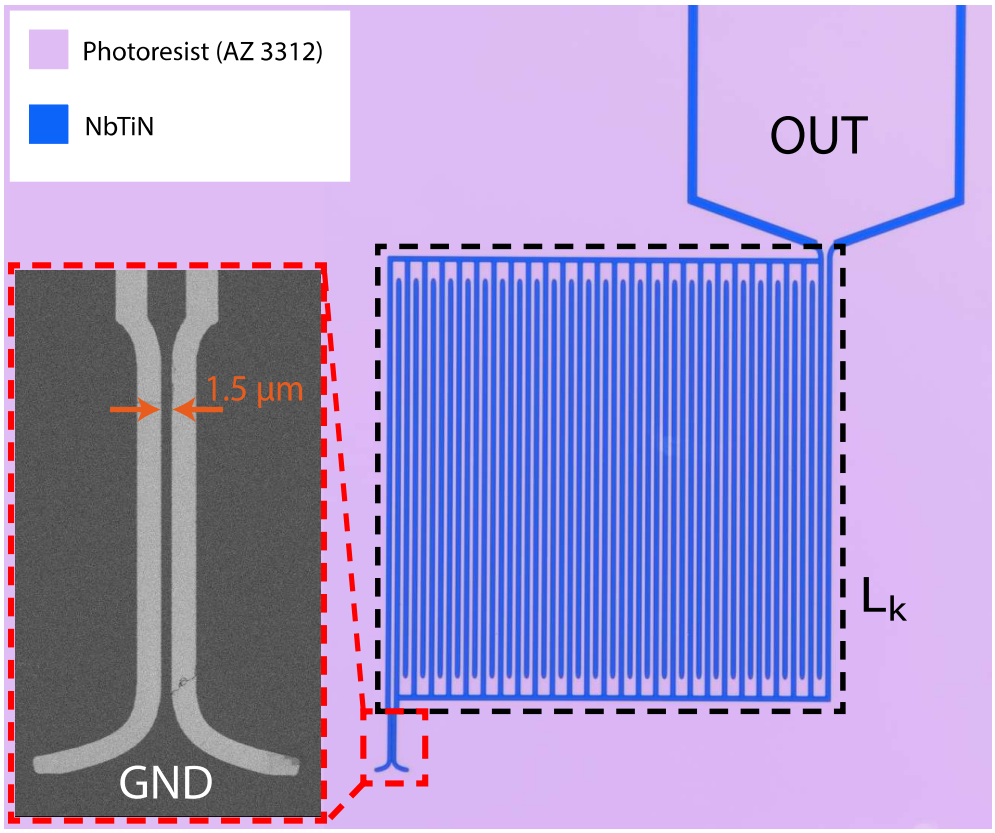


**Figure 4.5:** Micrograph of a micron-wide wire with a series 450 nH inductor, realized by patterning a 5.5-µm wide meandered wire on an area of 500 × 500 µm$^2$ highlighted by the black rectangle. Image was taken with photoresist on top of the structures to increase the contrast. **Inset**: SEM image of a 1.5 µm wide microstrip, the length is 50 µm, the image is taken at the end of the process, then the dark grey region represents NbTiN while light grey is the underlying $SiO_2$ layer.

that make it more sensible to the humidity or contamination in the lab, leading to severe constrictions. It is hard to believe that it is a design problem since no critical current was observed for a film with a $T_c$ which is more than the double of the working temperature. Alternatives, which are not film-dependent are a bad spreading of the GE varnish or bad mounting on the cryogenic stage, these were checked after the measurement and no significant errors were present.

# Chapter 5

# Conclusion and Future Outlook

## 5.1 Conclusion

In this work a process for deposition of superconducting NbTiN thin films by magnetron sputtering is proposed. For this work a $Nb_{0.5}Ti_{0.5}$ target was used in AJA International ATC Orion sputtering system. Resulting films showed a $T_c$ that is comparable with the room-temperature deposition of NbN but with a higher resistivity, which has been demonstrated to be an important parameter for high-performances SNSPDs. The effect of pressure and bias are analyzed showing that lower pressure enhances the $T_c$ of the films, without affecting the resistivity of the films, on the other hand the bias power leads to an increase of the $T_c$, but with significant lowering of the resistivity. The influence of $N_2$ variation has been studied proving a significant change in the resistivity of the films and $T_c$, showing a linear trend in the resistivity of the film with the $N_2$ flow. $N_2$ flow optimization for $T_c$ has been performed, using a set of 5-nm-thick films, showing a peak for a flow equal to 5.5 sccm and an abrupt decrease for flows $>$ 10 sccm. The Ar flow was set to 26.5 sccm. In addition, optical parameters have been studied for 5-nm-thick films showing a significant change in the optical properties of the film depending on the $N_2$ flow suggesting variation in crystalline order of the film. The $d$, $T_c$ and $R_s$ of the film were then fitted in a model which is valid for thin superconducting films, which links the $d$, $T_c$ and $R_s$ in the equation $dT_c = AR_s^B$. Parameters $A$ and $B$ were evaluated showing a possible dependence with $N_2$ flow (and then with interstitial N atoms).

A process for patterning sub-micron features has been developed, requiring both an optimization of dose and defocus given the thin positive-tone resist AZ 3312. Subsequently, an etching process has been developed for the complete removal of

residual resist, showing that post-exposure baking and thermal sinks are necessary for avoiding the burning of the photoresist.

At the end, a full electrical and optical characterization process for NbTiN micron-wide SMSPD wires in cryostats, using 1550 nm and 780 nm. The fabricated devices did not show a saturation in internal detection efficiency but it is possible to show that it is possible to realize single-photon sensitive large-area micron-wide structures.

## 5.2 Future experiments

### 5.2.1 Heated depositions

Another technique that was in plan was to sputter on heated samples, still using a bias, the temperature is supposed to increase the diffusivity of the sputtered material once the surface is reached, and, on the other side, the high temperature of the chamber close to the chip increases the reactivity of sputtered Nb and Ti with the nitrogen in the chamber, decreasing the interstitial N atoms or vacancies in the film, resulting in a more uniform film and favoring the crystalline order. For this reason, the resistivity of the film is expected to be lower, but on the other hand the critical temperature should go up. A trade-off between the temperature needed for enhancing sufficiently the critical temperature and the resistivity might be found. This technique can also be used for ultra-thin superconducting thin films, since 5-nm-thick films resulting in inability to realize a working SNSPD.
This experiment was not possible due to failure in the controller for the substrate-heating system.

### 5.2.2 Material characterization

Some deeper analysis in structure changes, due to $N_2$ concentration in the film may be run in future, for example by employing X-Ray Diffraction (XRD) techniques for estimating the size of the crystals in the films, since NbTiN is a polycristalline film, and evaluate possible effects on crystalline order due to low- or high-$N_2$ content.

# Appendix A

# Appendix

## A.1 Ellipsometry

Ellipsometry is a technique for measurement of thickness and optical parameters of thin films such as complex refractive index ($n + \mathrm{i}k$) or dielectric function. This versatile tool enables the characterization of composition, roughness, thickness (depth), crystalline nature, doping concentration, electrical conductivity, and various other material properties. It exhibits high sensitivity to changes in the optical response of incident radiation when interacting with the investigated material. This technique relies on measurement of the change in polarization due to reflection or transmission of a material, specifically along the s- and p-directions. The s- and p-directions are two orthogonal basis vectors used to express polarization states, where the p-direction is defined by the plane of incidence (the plane that contains incident and reflected beam and the vector normal to the sample surface. The s-direction is defined as the direction perpendicular to the p-direction, such as p-direction, s-direction and direction of propagation define a right-handed Cartesian coordinate system. From here, it is possible to define any totally polarized electromagnetic radiation, by defining the component of the electric filed along p- and s-direction, which are in general complex number, known as Jones vector.

$$\overrightarrow{E} = \begin{bmatrix} E_p \\ \\ E_s \end{bmatrix} \tag{A.1}$$

With the light expressed as a Jones vector, all light operations can now be represented using 2 x 2 transfer matrices, referred to as Jones matrices. This approach

facilitates the evaluation of optical components' effects within the instrument. Before reaching the sample, the light passes through a polarizer, ensuring the knowledge of its polarization state. Upon reflecting off the sample, the light encounters a continuously rotating analyzer before reaching the detector. The detector observes a sinusoidally varying intensity of light, dependent on the polarization state of the light reflected from the sample. To determine the intensity of light incident on the detector, the evaluation of the electric field is necessary, as intensity is proportional to the electric field of the light. To accomplish this, the Jones formalism is employed. By using the Jones formalism and considering the sample isotropic and not too rough, the beam of light incident on the detector, $E_D$ can be expressed as follows:

$$E_D = [\text{Analyzer matrix}][\text{Sample matrix}]\ [\text{Polarizer matrix}][\text{Input beam}] \quad \text{(A.2)}$$

where

$$\text{Polarizer matrix} = \begin{bmatrix} \cos P & -\sin P \\ \sin P & \cos P \end{bmatrix} \quad \text{(A.3)}$$

$$\text{Sample matrix} = \begin{bmatrix} R_p & 0 \\ 0 & R_s \end{bmatrix} \quad \text{(A.4)}$$

$$\text{Analyzer matrix} = \begin{bmatrix} 1 & 0 \\ 0 & 1 \end{bmatrix} \cdot \begin{bmatrix} \cos A & \sin A \\ -\sin A & \cos A \end{bmatrix} \quad \text{(A.5)}$$

From here it can be shown that:

$$E_D = \begin{bmatrix} R_p \cos P \cos A = R_s \sin P \sin A \\ 0 \end{bmatrix} \quad \text{(A.6)}$$

From this equation it is possible to define the complex ellipsometry ratio, $\rho$:

$$\rho \equiv \frac{R_p}{R_s} = \tan \Psi \exp(i\Delta) \tag{A.7}$$

# Bibliography


[1] Lixing You. Superconducting nanowire single-photon detectors for quantum information. *Nanophotonics*, 9(9):2673–2692, 2020.

[2] Matthew E. Grein, Andrew J. Kerman, Eric A. Dauler, Oleg Shatrovoy, Richard J. Molnar, Danna Rosenberg, Jung Yoon, Catherine E. DeVoe, Daniel V. Murphy, Bryan S. Robinson, and Don M. Boroson. Design of a ground-based optical receiver for the lunar laser communications demonstration. In *2011 International Conference on Space Optical Systems and Applications (ICSOS)*, pages 78–82, 2011.

[3] Feifei Wang, Fuqiang Ren, Zhuoran Ma, Liangqiong Qu, Ronan Gourgues, Chun Xu, Ani Baghdasaryan, Jiachen Li, Iman Esmaeil Zadeh, Johannes W. N. Los, Andreas Fognini, Jessie Qin-Dregely, and Hongjie Dai. In vivo non-invasive confocal fluorescence imaging beyond 1,700 nm using superconducting nanowire single-photon detectors. *Nature Nanotechnology*, 17(6):653–660, June 2022.

[4] Eleni Diamanti, Hoi-Kwong Lo, Bing Qi, and Zhiliang Yuan. Practical challenges in quantum key distribution. *npj Quantum Information*, 2(16025), 2016.

[5] Hiroki Takesue, Sae Woo Nam, Qiang Zhang, Robert H. Hadfield, Toshimori Honjo, Kiyoshi Tamaki, and Yoshihisa Yamamoto. Quantum key distribution over a 40-dB channel loss using superconducting single-photon detectors. *Nature Photonics*, 1(6):343–348, June 2007.

[6] Alberto Boaron, Gianluca Boso, Davide Rusca, Cedric Vulliez, Claire Autebert, Misael Caloz, Matthieu Perrenoud, Gaetan Gras, Felix Bussieres, Ming-Jun Li, Daniel Nolan, Anthony Martin, and Hugo Zbinden. Secure Quantum Key Distribution over 421 km of Optical Fiber. *Physical Review Letters*, 121(19):190502, November 2018.

[7] Hua-Lei Yin, Teng-Yun Chen, Zong-Wen Yu, Hui Liu, Li-Xing You, Yi-Heng Zhou, Si-Jing Chen, Yingqiu Mao, Ming-Qi Huang, Wei-Jun Zhang, Hao Chen, Ming Jun Li, Daniel Nolan, Fei Zhou, Xiao Jiang, Zhen Wang, Qiang Zhang, Xiang-Bin Wang, and Jian-Wei Pan. Measurement-Device-Independent Quantum Key Distribution Over a 404 km Optical Fiber. *Physical Review Letters*, 117(19):190501, November 2016.

[8] Veronika Parfentyeva, Lorenzo Colombo, Pranav Lanka, Marco Pagliazzi, Annalisa Brodu, Niels Noordzij, Jessie Qin-Dregely, Mirco Kolarczik, Alberto Dalla Mora, Davide Contini, Alessandro Toricelli, Turgut Durduran, and Antonio Pifferi. Fast in-vivo time-domain diffuse

correlation spectroscopy. In *Biophotonics Congress: Biomedical Optics 2022 (Translational, Microscopy, OCT, OTS, BRAIN)*, page OM4D.7. Optica Publishing Group, 2022.

[9] Nisan Ozana, Zavriyev Alexander I., Dibbyan Mazumder, Mitchell Robinson, Kutlu Kaya, Megan Blackwell, Stefan A. Carp, , and Maria Angela Franceschini. Superconducting nanowire single-photon sensing of cerebral blood flow. *Neurophotonics*, (035006), 2021.

[10] Alex D. Semenov, Gregory N. Goltsman, and Alexander A. Korneev. Quantum detection by current carrying superconducting film. *Physica C: Superconductivity*, 351(4):349–356, April 2001.

[11] G. N. Goltsman, O. Okunev, G. Chulkova, A. Lipatov, A. Semenov, K. Smirnov, B. Voronov, A. Dzardanov, C. Williams, and Roman Sobolewski. Picosecond superconducting single-photon optical detector. *Applied Physics Letters*, 79(6):705–707, August 2001.

[12] Chandra M Natarajan, Michael G Tanner, and Robert H Hadfield. Superconducting nanowire single-photon detectors: physics and applications. *Superconductor Science and Technology*, 25(6):063001, June 2012.

[13] R. Lusche, A. Semenov, K. Ilin, M. Siegel, Y. Korneeva, A. Trifonov, A. Korneev, G. Goltsman, D. Vodolazov, and H.-W. Hubers. Effect of the wire width on the intrinsic detection efficiency of superconducting-nanowire single-photon detectors. *Journal of Applied Physics*, 116(4):043906, July 2014.

[14] Marco Colangelo, Alexander B. Walter, Boris A. Korzh, Ekkehart Schmidt, Bruce Bumble, Adriana E. Lita, Andrew D. Beyer, Jason P. Allmaras, Ryan M. Briggs, Alexander G. Kozorezov, Emma E. Wollman, Matthew D. Shaw, and Karl K. Berggren. Large-Area Superconducting Nanowire Single-Photon Detectors for Operation at Wavelengths up to 7.4 µm. *Nano Letters*, 22(14):5667–5673, July 2022.

[15] D. Yu Vodolazov. Single-Photon Detection by a Dirty Current-Carrying Superconducting Strip Based on the Kinetic-Equation Approach. *Physical Review Applied*, 7(3):034014, March 2017.

[16] Jamie S. Luskin, Ekkehart Schmidt, Boris Korzh, Andrew D. Beyer, Bruce Bumble, Jason P. Allmaras, Alexander B. Walter, Emma E. Wollman, Lautaro Narvaez, Varun B. Verma, Sae Woo Nam, Ilya Charaev, Marco Colangelo, Karl K. Berggren, Cristian Pena, Maria Spiropulu, Maurice Garcia-Sciveres, Stephen Derenzo, and Matthew D. Shaw. Large active-area superconducting microwire detector array with single-photon sensitivity in the near-infrared. *Applied Physics Letters*, 122(24):243506, June 2023.

[17] J. Chiles, S. M. Buckley, A. Lita, V. B. Verma, J. Allmaras, B. Korzh, M. D. Shaw, J. M. Shainline, R. P. Mirin, and S. W. Nam. Superconducting microwire detectors based on WSi with single-photon sensitivity in the near-infrared. *Applied Physics Letters*, 116(24):242602, June 2020.

[18] I. Charaev, Y. Morimoto, A. Dane, A. Agarwal, M. Colangelo, and K. K. Berggren. Large-area microwire MoSi single-photon detectors at 1550 nm wavelength. *Applied Physics Letters*, 116(24):242603, June 2020.

[19] Yonit Hochberg, Ilya Charaev, Sae-Woo Nam, Varun Verma, Marco Colangelo, and Karl K. Berggren. Detecting Sub-GeV Dark Matter with Superconducting Nanowires. *Physical Review Letters*, 123(15):151802, October 2019.

[20] Dileep V. Reddy, Robert R. Nerem, Sae Woo Nam, Richard P. Mirin, and Varun B. Verma. Superconducting nanowire single-photon detectors with 98% system detection efficiency at 1550ââânm. *Optica*, 7(12):1649–1653, Dec 2020.

[21] J. Chang, J. W. N. Los, J. O. Tenorio-Pearl, N. Noordzij, R. Gourgues, A. Guardiani, J. R. Zichi, S. F. Pereira, H. P. Urbach, V. Zwiller, S. N. Dorenbos, and I. Esmaeil Zadeh. Detecting telecom single photons with $99.5^{2.07}_{+0.5}\%$ system detection efficiency and high time resolution. *APL Photonics*, 6(3):036114, March 2021.

[22] Boris Korzh, Qing-Yuan Zhao, Jason P. Allmaras, Simone Frasca, Travis M. Autry, Eric A. Bersin, Andrew D. Beyer, Ryan M. Briggs, Bruce Bumble, Marco Colangelo, Garrison M. Crouch, Andrew E. Dane, Thomas Gerrits, Adriana E. Lita, Francesco Marsili, Galan Moody, Cristian Pena, Edward Ramirez, Jake D. Rezac, Neil Sinclair, Martin J. Stevens, Angel E. Velasco, Varun B. Verma, Emma E. Wollman, Si Xie, Di Zhu, Paul D. Hale, Maria Spiropulu, Kevin L. Silverman, Richard P. Mirin, Sae Woo Nam, Alexander G. Kozorezov, Matthew D. Shaw, and Karl K. Berggren. Demonstration of sub-3 ps temporal resolution with a superconducting nanowire single-photon detector. *Nature Photonics*, 14(4):250–255, April 2020.

[23] Ioana Craiciu, Boris Korzh, Andrew D. Beyer, Andrew Mueller, Jason P. Allmaras, Lautaro Narvaez, Maria Spiropulu, Bruce Bumble, Thomas Lehner, Emma E. Wollman, and Matthew D. Shaw. High-speed detection of 1550 nm single photons with superconducting nanowire detectors. *Optica*, 10(2):183, February 2023.

[24] E. E. Wollman, V. B. Verma, A. D. Beyer, R. M. Briggs, B. Korzh, J. P. Allmaras, F. Marsili, A. E. Lita, R. P. Mirin, S. W. Nam, and M. D. Shaw. UV superconducting nanowire single-photon detectors with high efficiency, low noise, and 4 K operating temperature. *Optics Express*, 25(22):26792, October 2017.

[25] V. B. Verma, B. Korzh, A. B. Walter, A. E. Lita, R. M. Briggs, M. Colangelo, Y. Zhai, E. E. Wollman, A. D. Beyer, J. P. Allmaras, H. Vora, D. Zhu, E. Schmidt, A. G. Kozorezov, K. K. Berggren, R. P. Mirin, S. W. Nam, and M. D. Shaw. Single-photon detection in the mid-infrared up to 10 µm wavelength using tungsten silicide superconducting nanowire detectors. *APL Photonics*, 6(5):056101, May 2021.

[26] Yanqiu Guan, Haochen Li, Labao Zhang, Daxing Dong, Hao Wang, Qi Chen, Shuya Guo, Biao Zhang, Xiao Zhang, Zhuolin Yang, Xuecou Tu, Qingyuan Zhao, Xiaoqing Jia, Jian Chen, Lin Kang, and Peiheng Wu. Approaching pixel-level readout of SNSPD array by inductor-shaping pulse. *Applied Physics Letters*, 123(4):042602, July 2023.

[27] B. G. Oripov, D. S. Rampini, J. Allmaras, M. D. Shaw, S. W. Nam, B. Korzh, and A. N. McCaughan. A superconducting-nanowire single-photon camera with 400 000 pixels.

[28] Alessandro Buzzi, Matteo Castellani, Reed A. Foster, Owen Medeiros, Marco Colangelo, and Karl K. Berggren. A nanocryotron memory and logic family. *Applied Physics Letters*, 122(14):142601, April 2023.

[29] Reed A. Foster, Matteo Castellani, Alessandro Buzzi, Owen Medeiros, Marco Colangelo, and Karl K. Berggren. A superconducting nanowire binary shift register. *Applied Physics Letters*, 122(15):152601, April 2023.

[30] Daniel F. Santavicca, Marco Colangelo, Carleigh R. Eagle, Maitri P. Warusawithana, and Karl K. Berggren. 50 Ω transmission lines with extreme wavelength compression based on superconducting nanowires on high-permittivity substrates. *Applied Physics Letters*, 119(25):252601, December 2021.

[31] E. Toomey, K. Segall, M. Castellani, M. Colangelo, N. Lynch, and K. K. Berggren. Superconducting Nanowire Spiking Element for Neural Networks. *Nano Letters*, 20(11):8059–8066, November 2020.

[32] Philipp I. Zolotov, Alexander V. Semenov, Alexander V. Divochiy, Gregory N. Goltsman, Nikita R. Romanov, and Teunis M. Klapwijk. Dependence of Photon Detection Efficiency on Normal-State Sheet Resistance in *Marginally* Superconducting Films of NbN. *IEEE Transactions on Applied Superconductivity*, 31(5):1–5, August 2021.

[33] Lucy Elizabeth Archer. Optical properties of ultra-thin niobium nitride films for single photon detectors. 2017.

[34] Stephan Steinhauer, Lily Yang, Samuel Gyger, Thomas Lettner, Carlos Errando-Herranz, Klaus D. Jons, Mohammad Amin Baghban, Katia Gallo, Julien Zichi, and Val Zwiller. NbTiN thin films for superconducting photon detectors on photonic and two-dimensional materials. *Applied Physics Letters*, 116(17):171101, April 2020.

[35] Andrew E. Dane, Adam N. McCaughan, Di Zhu, Qingyuan Zhao, Chung-Soo Kim, Niccolo Calandri, Akshay Agarwal, Francesco Bellei, and Karl K. Berggren. Bias sputtered NbN and superconducting nanowire devices. *Applied Physics Letters*, 111(12):122601, September 2017.

[36] Pratiksha Pratap, Laxmipriya Nanda, Kartik Senapati, R P Aloysius, and Venugopal Achanta. Optimization of the superconducting properties of NbTiN thin films by variation of the $N_2$ partial pressure during sputter deposition. *Superconductor Science and Technology*, 36(8):085017, August 2023.

[37] P. Zolotov, S. Svyatodukh, A. Divochiy, V. Seleznev, and G. Goltsman. High-resistivity niobium nitride films for saturated-efficiency SMSPDs at telecom wavelengths and beyond. *Applied Physics Letters*, 122(15):152602, April 2023.

[38] Owen Medeiros. Investigation of thin film supercurrent and photodetection in wide niobium nitride wires. 2022.

[39] Yachin Ivry, Chung-Soo Kim, Andrew E. Dane, Domenico De Fazio, Adam N. McCaughan, Kristen A. Sunter, Qingyuan Zhao, and Karl K. Berggren. Universal scaling of the critical temperature for thin films near the superconducting-to-insulating transition. *Physical Review B*, 90(21):214515, December 2014.

[40] Archan Banerjee, Robert M. Heath, Dmitry Morozov, Dilini Hemakumara, Umberto Nasti, Iain Thayne, and Robert H. Hadfield. Optical properties of refractory metal based thin films. *Optical Materials Express*, 8(8):2072, August 2018.

[41] Glenn Martinez. Towards saturation of detection efficiency in superconducting single photon detectors at 4.2 K using local helium ion irradiation. 2021.

[42] M. Ejrnaes, C. Cirillo, D. Salvoni, F. Chianese, C. Bruscino, P. Ercolano, A. Cassinese, C. Attanasio, G. P. Pepe, and L. Parlato. Single photon detection in NbRe superconducting microstrips. *Applied Physics Letters*, 121(26):262601, December 2022.

[43] Maximilian Protte, Varun B Verma, Jan Philipp Hopker, Richard P Mirin, Sae Woo Nam, and Tim J Bartley. Laser-lithographically written micron-wide superconducting nanowire single-photon detectors. *Superconductor Science and Technology*, 35(5):055005, May 2022.

[44] Masahiro Yabuno, Fumihiro China, Shigehito Miki, and Hirotaka Terai. Large-Area Niobium Titanium Nitride Superconducting Microstrip Single-Photon Detector Fabricated Using a Photolithography Process. *IEEE Transactions on Applied Superconductivity*, 33(5):1–4, August 2023.

[45] Yu-Ze Wang, Wei-Jun Zhang, Guang-Zhao Xu, Jia-Min Xiong, Dong-Hui Fan, Zhi-Gang Chen, Xing-Yu Zhang, Zhen Wang, and Li-Xing You. Characterization of a superconducting microstrip single-photon detector shunted with an external resistor. *Superconductor Science and Technology*, 36(6):065004, June 2023.

[46] S.M. Buckley, A.N. Tait, J. Chiles, A.N. McCaughan, S. Khan, R.P. Mirin, S.W. Nam, and J.M. Shainline. Integrated-Photonic Characterization of Single-Photon Detectors for Use in Neuromorphic Synapses. *Physical Review Applied*, 14(5):054008, November 2020.

[47] Xiaorong Gu, Kun Huang, Haifeng Pan, E Wu, and Heping Zeng. Efficient mid-infrared single-photon frequency upconversion detection with ultra-low background counts. *Laser Physics Letters*, 10(5):055401, May 2013.